

Dynamics of a surfactant-laden viscoelastic thread in the presence of surface viscosity

Fang Li¹ and Dongdong He^{2,†}

¹Department of Modern Mechanics, University of Science and Technology of China, Hefei, Anhui 230027, PR China

²School of Science and Engineering, The Chinese University of Hong Kong, Shenzhen, Guangdong, 518172, PR China

(Received 24 October 2022; revised 20 February 2023; accepted 28 May 2023)

As is known, the presence of surfactants can profoundly influence the dynamics of Newtonian viscous threads. Also, it is known that non-Newtonian viscoelastic threads behave differently from Newtonian ones, particularly in the nonlinear regime. A naturally arising question is how surfactants affect the dynamic behaviour of non-Newtonian viscoelastic threads. To gain some insights into it, we build a one-dimensional model for an Oldroyd-B/finitely extensible nonlinear elastic-Peterlin approximation (FENE-P) viscoelastic liquid thread covered with an insoluble surfactant monolayer based on the slender body theory. A parametric study is performed to examine the effects of the dimensionless numbers related to the surfactant, including the initial concentration, the Marangoni number, the surface Péclet number, the shear Boussinesq number and the dilatational Boussinesq number. It is found that the formation of the beads-on-a-string structure can be greatly delayed by the surfactant. At large values of the surface Péclet number, the exponential thinning of the Oldroyd-B viscoelastic thread is little influenced, but the surfactant may lead to the disappearance of secondary droplets. At moderate values of the surface Péclet number, the surfactant induces the formation of secondary droplets. The primary droplets are axially stretched by the Marangoni or surface viscous stresses and evolve into a prolate or a more singular shape eventually. The surfactant can delay the pinch-off of the FENE-P viscoelastic thread to a great extent, but it affects little the decrease in the minimum thread radius prior to pinch-off when the surface Péclet number is large.

Key words: nonlinear instability, viscoelasticity, slender-body theory

† Email address for correspondence: hedongdong@cuhk.edu.cn

1. Introduction

The presence of surface active agents (surfactants) can significantly alter the surface properties of a liquid and give rise to interesting phenomena, such as tip streaming from a highly deformed liquid droplet submerged in a shear or extensional flow (Eggers 1997; Anna 2016; Montanero & Gañán-Calvo 2020) and flower-like patterning of an evaporating liquid droplet spreading on a liquid substrate (Wodlei *et al.* 2018). In a variety of applications including atomization, ink-jet printing, spinning, coating, emulsification, enhanced oil recovery, microfluidics, food industry and drug delivery, the addition of surfactant molecules can help to control actively and easily the motion, spread, transport, formation, deformation and breakup of films, jets, threads, drops, bubbles, colloids or biological molecules. Surfactants have been one of the most attractive and most studied factors in those liquid–air surface and liquid–liquid interfacial problems in the last three decades (Eggers & Villermaux 2008; Vlahovska 2019; Montanero & Gañán-Calvo 2020). Nevertheless, the underlying mechanisms have not yet been fully understood.

An insoluble surfactant monolayer at a liquid surface may affect the dynamics of the liquid in three ways (Kamat *et al.* 2018; Montanero & Gañán-Calvo 2020; Wee, Wagoner & Basaran 2022): it lowers the average capillary force by reducing the surface tension coefficient, i.e. the so-called soluto-capillarity effect; the non-uniform distribution of surfactant molecules at the surface causes a non-zero surface tension gradient and thereby the Marangoni stress that tends to eliminate the non-uniformity; it induces the surface rheological effects characterized by the surface shear and dilatational viscosities, and with shear and dilatational deformations of the surface, it yields the viscous stresses that participate in the force balance at the surface. The reduction in the surface tension, the surface tension gradient and the resulting Marangoni stress and the surface viscous stresses are all associated with the distribution of surfactant at the surface. The distribution of insoluble surfactant is basically determined by two mechanisms: surface convection and surface diffusion. The former gives rise to inhomogeneity and thereby surface tension gradients, whereas the latter tends to restore homogeneity (Hameed *et al.* 2008; Martínez-Calvo & Sevilla 2018; Montanero & Gañán-Calvo 2020). The relative importance of surface convection and surface diffusion, represented by the surface Péclet number, may substantially influence the dynamics of a fluid system. In general, the multiple effects of a surfactant monolayer together with their complex mathematical descriptions make the related theoretical, numerical and experimental investigations challenging.

The situation can be more intricate when the surfactant is soluble. In such a case, surfactant molecules exist not only at the surface but also in the bulk. The solubility cannot be neglected when the adsorption/desorption characteristic time of the surfactant is comparable to or smaller than the other characteristic times of the system (e.g. the capillary time for a Newtonian jet or both the capillary time and the extensional relaxation time for a viscoelastic jet). If the bulk concentration of the surfactant is below the critical micellar concentration (CMC), it is presented as monomers in the bulk; if the bulk concentration is above the CMC, surfactant molecules partially aggregate into micelles spontaneously (Craster, Matar & Papageorgiou 2009; Montanero & Gañán-Calvo 2020). The concentrations of monomers and micelles are governed by their respective conservation equations. There is a term describing the breakup or formation of micelles in each equation. Moreover, there is a term denoting the flux of surfactant from the bulk to the surface due to the adsorption/desorption process in the conservation equation at the surface. Surfactant solubility seems to affect fluid dynamics in an indirect way.

Studying how capillarity, bulk viscosity, inertia, Marangoni stress, surface viscosity and other possible factors compete with or cooperate with each other in a fluid system has both scientific and practical relevance. There have been many reports in the literature devoted to understanding the effects of insoluble or soluble surfactants on the linear and nonlinear dynamics of films, drops, bubbles, jets, threads and other similar configurations, e.g. Liao, Franses & Basaran (2006), Hameed *et al.* (2008), Craster *et al.* (2009), Young *et al.* (2009), Ponce-Torres *et al.* (2016), Martínez-Calvo & Sevilla (2018), Hu, Fu & Yang (2020), He & Wylie (2021) and Wee *et al.* (2021). The mechanism in one geometric configuration may be extrapolated to another. It is also possible that different mechanisms play a major role in different configurations. In the following, we introduce the studies of cylindrical liquid jets and threads.

Linear theory has confirmed that the presence of surfactants has a stabilizing effect on the Rayleigh–Plateau instability of Newtonian viscous liquid jets (Craster, Matar & Papageorgiou 2002; Timmermans & Lister 2002; Ponce-Torres *et al.* 2016; Martínez-Calvo & Sevilla 2018). That is, surfactants reduce the growth rates of small disturbances. This effect is unsurprising, since the average capillary force is lowered and the Marangoni and surface viscous stresses are created in the presence of surfactants. Similarly, increasing surfactant activity or surface viscosity stabilizes liquid jets. Another finding is that the linear analysis based on the long wave approximation cannot accurately predict some instability features (such as the cutoff wavenumber) of surfactant-laden liquid jets and threads without the inclusion of the necessary high-order terms (Hansen, Peters & Meijer 1999; Timmermans & Lister 2002; Martínez-Calvo & Sevilla 2018).

The nonlinear effects come into play, as disturbances grow with time. Linear theory fails to predict the late stages of jet or thread instability. The nonlinear dynamics of Newtonian jets and threads in the presence of surfactants has been studied via the asymptotic methods and numerical simulations, e.g. Anshus (1973), Craster *et al.* (2002), Timmermans & Lister (2002), Dravid *et al.* (2006), McGough & Basaran (2006), Craster *et al.* (2009), Hameed & Maldarelli (2016), Martínez-Calvo *et al.* (2020) and Wee *et al.* (2021). It was found that the pinch-off of Newtonian liquid threads can be delayed by surfactants (Anshus 1973; Craster *et al.* 2002). The addition of surfactants to Newtonian viscous threads favours the formation of secondary droplets between primary droplets. The size of secondary droplets is increased or decreased by surfactants, depending on their strength and diffusivity (Dravid *et al.* 2006). Surface viscosities were found to be responsible for the accumulation of surfactant molecules in secondary droplets (Ponce-Torres *et al.* 2016, 2017). The detachment of primary droplets will never take place and the formation of secondary droplets will be impeded, as long as the Marangoni stress is sufficiently large (Hameed *et al.* 2008). The experimental and numerical studies of McGough & Basaran (2006) and Kamat *et al.* (2018) showed that the Marangoni stress near the pinching point of a thread induces the formation of microthread cascades. When the transport of an insoluble surfactant is dominated by surface convection (the surface Péclet number is large), surfactant molecules are swept away from the pinching point (Newtonian liquid threads pinch off at the neck where the primary droplet joins the ligament). As a result, surfactant-laden jets behave in a similar way to surfactant-free jets prior to pinch-off and exhibit the same similarity (Eggers 1993; Craster *et al.* 2002; Timmermans & Lister 2002; Liao *et al.* 2006; McGough & Basaran 2006; Eggers & Villermaux 2008). Remarkably, the surface viscous stresses can still play a role when most of surfactant molecules are swept away from the pinching point, because the surface-to-volume ratio at the pinching point becomes extremely large as the minimum radius of the jet tends to zero (Montanero & Gañán-Calvo 2020; Wee *et al.* 2020, 2021). However, surfactant molecules are not always evacuated from the pinching region, even for large surface Péclet numbers of the order

of 10^5 , as detected by Ponce-Torres *et al.* (2020). The one-dimensional (1-D) nonlinear analysis of surfactant-laden viscous threads in the Stokes limit showed that there exists a critical value of the surface Péclet number. Below this critical value, surface diffusion is dominant and the thread thins exponentially in time; above it, surface convection is dominant and the thinning of the thread exhibits a power-law dependence on time until pinch-off (Wee *et al.* 2022). In the Stokes limit, the surface viscous stresses enter the dominant force balance and tend to slow down the thinning of Newtonian threads (Ozan & Jakobsen 2019; Wee *et al.* 2020). The balance between the capillary force and the surface viscous stresses is established at sufficiently high surfactant surface concentrations, resulting in an asymptotic regime in which the filament thins exponentially in time at a rate only depending on the surface tension and the surface viscosities (Martínez-Calvo & Sevilla 2020). When the inertia is taken into account, the inertial, capillary, bulk viscous and surface viscous forces establish the dominant force balance as the jet nears pinch-off, whereas the Marangoni stress plays a secondary role (Wee *et al.* 2021). For viscous threads laden with soluble surfactants at concentrations above the CMC, larger secondary droplets are formed due to the Marangoni stress (Craster *et al.* 2009). The study of the surfactant effects has been extended to compound liquid jets (Craster, Matar & Papageorgiou 2003; Yao, Yang & Fu 2021).

Polymer solutions are frequently encountered in applications. They belong to the family of non-Newtonian fluids, possessing rheological properties such as shear thinning and viscoelasticity. A dilute polymer solution can be approximately regarded as a viscoelastic liquid of constant viscosity (Tirtaatmadja, McKinley & Cooper-White 2006; James 2009). Thus the elastic effects are separated from the viscous effects, greatly facilitating the study of the viscoelastic liquid dynamics. The linear and nonlinear behaviour of viscoelastic liquid jets and threads has been studied analytically and numerically with the aid of simple viscoelastic models such as Oldroyd-B, Giesekus and finitely extensible nonlinear elastic (Goldin *et al.* 1969; Goren & Gottlieb 1982; Entov & Hinch 1997; Chang, Demekhin & Kalaidin 1999; Brenn, Liu & Durst 2000; Fontelos & Li 2004; Clasen *et al.* 2006a; Liu & Liu 2006; Eggers & Villermaux 2008; Ardekani, Sharma & Mckinley 2010; Bhat *et al.* 2010; Ye, Yang & Fu 2016; Turkoz *et al.* 2018; Alsharif 2019). In the linear regime, viscoelastic jets were found to be more unstable than their Newtonian counterparts when the axial viscoelastic stress in the base flow is relaxed sufficiently far away from the nozzle. In the nonlinear regime, phenomenally different from Newtonian jets, viscoelastic jets evolve into a quasistatic topological structure, i.e. the beads-on-a-string structure, which is characterized by primary droplets connected by a thin filament of almost uniform thickness (sometimes secondary droplets exist in the filament). The pinch-off of viscoelastic liquid threads, if it occurs in finite time, can be greatly delayed by viscoelasticity. Note that the aforementioned viscoelastic models possess a constant viscosity and a single relaxation time and cannot account for the concentration dependence or the conformation dependence of the viscosity or the relaxation time (Beck & Shaqfeh 2006; Clasen *et al.* 2006b; Prabhakar, Prakash & Sridhar 2006; Tirtaatmadja *et al.* 2006; Dinic & Sharma 2020; Kumar, Richter & Schroeder 2020). As a consequence, they may fail to capture accurately the capillary thinning or pinching dynamics of viscoelastic threads observed in experiments. Future theoretical and numerical studies are expected to consider more realistic models.

The addition of soluble surfactants to polymer solutions may introduce additional complexity and difficulty in mathematical formulation and experimental measurement (Martínez Narváez, Mazur & Sharma 2021). On the one hand, surfactants may influence the rheological properties of polymer solutions to a certain extent, for example, increasing bulk viscosity and lowering the critical shear rate for the onset of shear thinning.

On the other hand, the interaction between polymer molecules and surfactant molecules may lead to the self-aggregation of the latter above the critical aggregation concentration when the bulk concentration of surfactant is sufficiently high. To date, the dynamics of polymer–surfactant association complexes has been rarely reported. An experimental investigation was executed by Dechelette *et al.* (2011) to examine the combined effect of polymer and soluble surfactant on the jet breakup and secondary droplet formation. It was found that the Marangoni stress may lead to an increase in secondary droplet size at sufficiently high surfactant concentrations.

If the surfactant has a negligible solubility or is insoluble, the interaction between polymer and surfactant molecules can be appropriately neglected. Even for this much simpler case, few studies can be found in the literature addressing the dynamics of surfactant-laden viscoelastic liquid jets or threads. An asymptotic approach based on the slenderness of the jet was used by Alhushaybari & Uddin (2020) to study the absolute and convective instability of a viscoelastic liquid jet falling under the gravity in the presence of insoluble surfactants. They identified the convective/absolute instability boundaries for various parameter regimes. He & Wylie (2021) studied the temporal linear instability of a viscoelastic thread surrounded by another immiscible viscoelastic fluid in the presence of insoluble surfactants. They carried out a detailed parametric study and concluded that the surfactant decreases the growth rates and increases the most unstable wavenumber corresponding to the maximum growth rate.

At the nonlinear stages, viscoelastic liquid jets and threads behave differently from Newtonian ones, particularly the delay of pinch-off and the formation of the beads-on-a-string structure. To our knowledge, the effect of surfactants on the nonlinear characteristics of viscoelastic liquid jets and threads has not yet been reported. In the present work, we build a 1-D model to describe the nonlinear dynamic behaviour of viscoelastic threads in the presence of insoluble surfactants, taking into account the surface rheological effects. A number of 1-D models based on the slender body theory have been developed for clean Newtonian viscous threads, surfactant-laden Newtonian viscous threads or clean viscoelastic threads (Eggers & Villermaux 2008; Montanero & Gañán-Calvo 2020). It has been shown that these simplified 1-D models provide reasonable results at a much lower computational cost than the two-dimensional (2-D) and three-dimensional (3-D) numerical simulations.

The paper is organized as follows: in § 2, the theoretical model is described; in § 3, the 1-D equations are derived; in § 4, the dispersion relation for the 1-D linear analysis is derived and a parametric study is performed to examine the effects of the surfactant on the linear and nonlinear behaviour of the viscoelastic thread; finally, in § 5, the main conclusion is drawn.

2. Theoretical description

Consider an infinitely long cylindrical liquid thread of radius R surrounded by atmospheric air, as sketched in figure 1. The liquid, which is a polymer solution, is incompressible and viscoelastic. Before being perturbed, the thread is quiescent with no base flow, and moreover, the thread surface is covered uniformly with a monolayer of bulk-insoluble surfactant molecules of concentration Γ_0 . The rheological properties of the surfactant, characterized by the surface shear and dilatational viscosities, are taken into account. The hydrodynamic effect of the ambient air is neglected. The effect of the gravitational force, temperature and mass transfer is neglected as well. The cylindrical coordinate system (z, r, θ) with z, r, θ the axial, radial and azimuthal coordinates, respectively, is used to describe the problem. Upon a small-amplitude axisymmetric harmonic

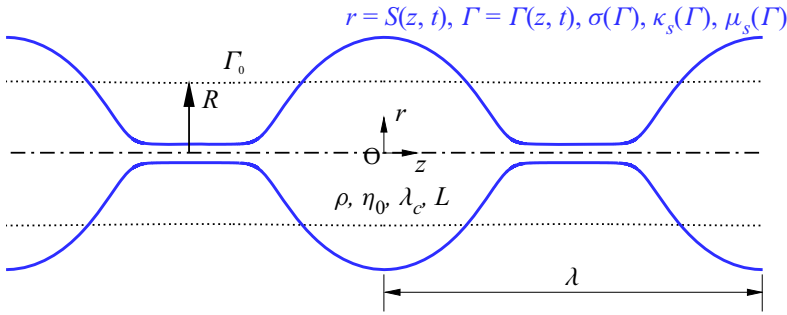


Figure 1. Schematic of a viscoelastic liquid thread covered with an insoluble surfactant.

disturbance being imposed, the thread begins to deform, whose shape is denoted by $r = S(z, t)$. Simultaneously, the surfactant is redistributed along the thread surface, whose concentration is denoted by $\Gamma = \Gamma(z, t)$.

The continuity and momentum equations governing the flow field are

$$\frac{1}{r} \frac{\partial(rv)}{\partial r} + \frac{\partial u}{\partial z} = 0, \tag{2.1}$$

$$\begin{aligned} \rho \left(\frac{\partial v}{\partial t} + v \frac{\partial v}{\partial r} + u \frac{\partial v}{\partial z} \right) = & -\frac{\partial p}{\partial r} + \eta_s \left(\frac{\partial^2 v}{\partial r^2} + \frac{1}{r} \frac{\partial v}{\partial r} - \frac{v}{r^2} + \frac{\partial^2 v}{\partial z^2} \right) \\ & + \frac{\partial \tau_{rr}}{\partial r} + \frac{\partial \tau_{rz}}{\partial z} + \frac{\tau_{rr} - \tau_{\theta\theta}}{r}, \end{aligned} \tag{2.2}$$

$$\rho \left(\frac{\partial u}{\partial t} + v \frac{\partial u}{\partial r} + u \frac{\partial u}{\partial z} \right) = -\frac{\partial p}{\partial z} + \eta_s \left(\frac{\partial^2 u}{\partial r^2} + \frac{1}{r} \frac{\partial u}{\partial r} + \frac{\partial^2 u}{\partial z^2} \right) + \frac{\partial \tau_{rz}}{\partial r} + \frac{\tau_{rz}}{r} + \frac{\partial \tau_{zz}}{\partial z}, \tag{2.3}$$

where u and v are the axial and radial components of the velocity vector \mathbf{u} , respectively, ρ is the density of the polymer solution, p is the pressure, η_s is the contribution of the solvent to the viscosity and τ_{zz} , τ_{rr} , τ_{rz} and $\tau_{\theta\theta}$ are the components of the polymer stress tensor $\boldsymbol{\tau}_p$ which, in the form of a matrix, is

$$\boldsymbol{\tau}_p = \begin{pmatrix} \tau_{zz} & \tau_{rz} & 0 \\ \tau_{rz} & \tau_{rr} & 0 \\ 0 & 0 & \tau_{\theta\theta} \end{pmatrix}. \tag{2.4}$$

The viscoelasticity of the liquid is assumed to be described by the FENE-P (finitely extensible nonlinear elastic-Peterlin approximation) constitutive equation (Fontelos & Li 2004)

$$\boldsymbol{\tau}_p = \frac{\eta_p}{\lambda_c} \left(\frac{\mathbf{A}}{1 - \frac{tr(\mathbf{A})}{L^2}} - \mathbf{I} \right), \tag{2.5}$$

where η_p is the contribution of the polymer to the viscosity, λ_c is the stress relaxation time, L is the finite extensibility parameter, \mathbf{I} is the identity tensor, \mathbf{A} is the conformation tensor

whose components are

$$\mathbf{A} = \begin{pmatrix} A_{zz} & A_{rz} & 0 \\ A_{rz} & A_{rr} & 0 \\ 0 & 0 & A_{\theta\theta} \end{pmatrix}, \quad (2.6)$$

and $tr(\mathbf{A})$ is the trace of \mathbf{A} . The four non-zero components of \mathbf{A} are governed by

$$\frac{\partial A_{zz}}{\partial t} + v \frac{\partial A_{zz}}{\partial r} + u \frac{\partial A_{zz}}{\partial z} = 2 \frac{\partial u}{\partial z} A_{zz} + 2 \frac{\partial u}{\partial r} A_{rz} + \frac{1}{\lambda_c} \left(1 - \frac{A_{zz}}{1 - \frac{tr(\mathbf{A})}{L^2}} \right), \quad (2.7)$$

$$\frac{\partial A_{rr}}{\partial t} + v \frac{\partial A_{rr}}{\partial r} + u \frac{\partial A_{rr}}{\partial z} = 2 \frac{\partial v}{\partial r} A_{rr} + 2 \frac{\partial v}{\partial z} A_{rz} + \frac{1}{\lambda_c} \left(1 - \frac{A_{rr}}{1 - \frac{tr(\mathbf{A})}{L^2}} \right), \quad (2.8)$$

$$\frac{\partial A_{\theta\theta}}{\partial t} + v \frac{\partial A_{\theta\theta}}{\partial r} + u \frac{\partial A_{\theta\theta}}{\partial z} = 2 \frac{v}{r} A_{\theta\theta} + \frac{1}{\lambda_c} \left(1 - \frac{A_{\theta\theta}}{1 - \frac{tr(\mathbf{A})}{L^2}} \right), \quad (2.9)$$

$$\frac{\partial A_{rz}}{\partial t} + v \frac{\partial A_{rz}}{\partial r} + u \frac{\partial A_{rz}}{\partial z} = \frac{\partial v}{\partial z} A_{zz} + \frac{\partial u}{\partial r} - \frac{v}{r} A_{rz} + \frac{1}{\lambda_c} \left(- \frac{A_{rz}}{1 - \frac{tr(\mathbf{A})}{L^2}} \right). \quad (2.10)$$

The surfactant concentration Γ is governed by the time-dependent advection–diffusion equation (Hameed *et al.* 2008; Martínez-Calvo & Sevilla 2018)

$$\frac{\partial \Gamma}{\partial t} + u \frac{\partial \Gamma}{\partial z} + \frac{\Gamma}{S\sqrt{1+S'^2}} \frac{\partial(Su_t)}{\partial z} + C\Gamma u_n = \frac{D_s}{S\sqrt{1+S'^2}} \frac{\partial \left(\frac{S\Gamma'}{\sqrt{1+S'^2}} \right)}{\partial z}, \quad (2.11)$$

where the prime ' denotes the partial derivative with respect to z , D_s is the surface diffusion coefficient of the surfactant, u_n and u_t are the normal and tangential components of the velocity at the surface, i.e.

$$u_n = \frac{v - uS'}{\sqrt{1+S'^2}}, \quad u_t = \frac{u + vS'}{\sqrt{1+S'^2}}, \quad (2.12a,b)$$

and C is the mean curvature given by

$$C = \frac{1}{S\sqrt{1+S'^2}} - \frac{S''}{(1+S'^2)^{3/2}}, \quad (2.13)$$

with '' denoting the second-order derivative with respect to z .

At the thread surface $r = S(z, t)$, the kinematic condition must be satisfied, i.e.

$$v = \frac{\partial S}{\partial t} + u \frac{\partial S}{\partial z}, \quad (2.14)$$

and the force balance requires

$$-\mathbf{T} \cdot \mathbf{n} + \nabla_s \cdot \mathbf{T}_s = 0, \quad (2.15)$$

where $\mathbf{T} = -p\mathbf{I} + \eta_s[\nabla\mathbf{u} + (\nabla\mathbf{u})^T] + \boldsymbol{\tau}_p$ is the stress tensor from the liquid phase but evaluated at the thread surface (the superscript T indicates the transpose), \mathbf{n} is the

unit outward vector normal to the surface, ∇_s is the surface gradient operator defined as $\nabla_s = \mathbf{I}_s \cdot \nabla = (\mathbf{I} - \mathbf{nn}) \cdot \nabla$ and \mathbf{T}_s is the surface stress tensor modelled by the Boussinesq–Scriven approximation (Boussinesq 1913; Scriven 1960; Martínez-Calvo & Sevilla 2018)

$$\mathbf{T}_s = \mathbf{I}_s[\sigma + (\kappa_s - \mu_s)(\nabla_s \cdot \mathbf{u}_s)] + \mu_s[(\nabla_s \mathbf{u}_s) \cdot \mathbf{I}_s + \mathbf{I}_s \cdot (\nabla_s \mathbf{u}_s)^T], \quad (2.16)$$

where κ_s and μ_s are the surface dilatational and shear viscosities, respectively, \mathbf{u}_s is the velocity of the polymer solution at the surface and σ is the surface tension coefficient (hereafter, it is called the surface tension for short). Note that κ_s , μ_s and σ are all functions of the local surfactant concentration Γ . We simply assume that κ_s and μ_s are linearly dependent on Γ (Ponce-Torres *et al.* 2017; Wee *et al.* 2021), i.e.

$$\kappa_s(\Gamma) = \kappa_{sr} \frac{\Gamma}{\Gamma_r}, \quad \mu_s(\Gamma) = \mu_{sr} \frac{\Gamma}{\Gamma_r}, \quad (2.17a,b)$$

where the subscript r denotes the reference values. The dependence of the surface tension σ on the surfactant surface concentration Γ is assumed to be described by the Langmuir equation of state (Liao *et al.* 2006; Hameed *et al.* 2008; Wee *et al.* 2021)

$$\sigma(\Gamma) = \sigma_0 + R_g T \Gamma_\infty \ln \left(1 - \frac{\Gamma}{\Gamma_\infty} \right), \quad (2.18)$$

where σ_0 is the surface tension of the clean surface, R_g is the universal gas constant, T is the absolute temperature and Γ_∞ is the maximum packing concentration of the surfactant. Introducing the surface pressure $\Pi(\Gamma) = \sigma_0 - \sigma(\Gamma)$, the combination of (2.17a,b) and (2.18) gives the following dependence

$$\kappa_s(\Pi) = \kappa_{sr} \frac{\Gamma_\infty}{\Gamma_r} \left[1 - \exp \left(-\frac{\Pi}{R_g T \Gamma_\infty} \right) \right], \quad \mu_s(\Pi) = \mu_{sr} \frac{\Gamma_\infty}{\Gamma_r} \left[1 - \exp \left(-\frac{\Pi}{R_g T \Gamma_\infty} \right) \right]. \quad (2.19a,b)$$

As a matter of fact, the dependence of the surface viscosities on the surface pressure diverges. For instance, it was found in the experiments that the surface shear viscosity μ_s often increases exponentially with the surface pressure Π (Fuller & Vermant 2012; Manikantan & Squires 2020). The Π -dependent surface viscosities have been shown to lead to surprising consequences in lubrication flows and affect significantly the deformation and breakup of droplets (Manikantan & Squires 2017; Singh & Narsimhan 2021, 2022; Herrada *et al.* 2022). They may also affect the dynamics of liquid jets and threads, which remains an open problem to be explored.

The substitution of (2.16) into (2.15) yields

$$\begin{aligned} & -\mathbf{T} \cdot \mathbf{n} + \nabla_s \sigma - \mathbf{n}(\nabla_s \cdot \mathbf{n})\sigma + \nabla_s [(\kappa_s - \mu_s)(\nabla_s \cdot \mathbf{u}_s)] \\ & - \mathbf{n}(\nabla_s \cdot \mathbf{n})(\kappa_s - \mu_s)(\nabla_s \cdot \mathbf{u}_s) + \nabla_s \cdot \left\{ \mu_s \left[(\nabla_s \mathbf{u}_s) \cdot \mathbf{I}_s + \mathbf{I}_s \cdot (\nabla_s \mathbf{u}_s)^T \right] \right\} = 0. \end{aligned} \quad (2.20)$$

After some algebraic operations, the force balance in the normal direction is written as

$$\begin{aligned} & p - \frac{1}{1 + S^2} \left[2\eta_s \frac{\partial v}{\partial r} - 2\eta_s \left(\frac{\partial v}{\partial z} + \frac{\partial u}{\partial r} \right) + 2\eta_s S'^2 \frac{\partial u}{\partial z} + S'^2 \tau_{zz} - 2S' \tau_{rz} + \tau_{rr} \right] \\ & = \mathcal{C} \left[\sigma + (\kappa_s - \mu_s) \left(\frac{(Su_t)'}{S\sqrt{1 + S'^2}} + \mathcal{C}u_n \right) \right] \\ & + \frac{2\mu_s}{1 + S'^2} \left[\frac{S'u_t + u_n}{S^2} - \frac{S''}{1 + S'^2} \left(\frac{\partial(u_t)}{\partial z} - \frac{S''u_n}{1 + S'^2} \right) \right], \end{aligned} \quad (2.21)$$

and in the tangential direction as

$$\begin{aligned}
 & \frac{1}{\sqrt{1+S'^2}} \left[2\eta_s S' \left(\frac{\partial v}{\partial r} - \frac{\partial u}{\partial z} \right) + \eta_s (1-S'^2) \left(\frac{\partial v}{\partial z} + \frac{\partial u}{\partial r} \right) \right. \\
 & \quad \left. + S' (\tau_{rr} - \tau_{zz}) + (1-S'^2)\tau_{rz} \right] \\
 & = \frac{\partial \sigma}{\partial z} + \frac{\partial}{\partial z} \left[(\kappa_s - \mu_s) \left(\frac{(Su_t)'}{S\sqrt{1+S'^2}} + Cu_n \right) \right] \\
 & \quad + \frac{\sqrt{1+S'^2}}{S} \frac{\partial}{\partial z} \left[\frac{2\mu_s S}{1+S'^2} \left(\frac{\partial u_t}{\partial z} - \frac{u_n S''}{1+S'^2} \right) \right] \\
 & \quad - \frac{2\mu_s S'}{\sqrt{1+S'^2}} \left[\frac{S'u_t + u_n}{S^2} - \frac{S''}{1+S'^2} \left(\frac{\partial u_t}{\partial z} - \frac{S''u_n}{1+S'^2} \right) \right]. \tag{2.22}
 \end{aligned}$$

3. One-dimensional model

If the radius of the perturbed thread varies gradually along the axial direction, the thread can be considered as a slender body and a 1-D analysis can be applied (Clasen *et al.* 2006a; Eggers & Villermaux 2008). The equations for the 1-D model are derived in Appendix A.

Taking the thread radius R , the capillary time $t_c = \sqrt{\rho R^3/\sigma_0}$, the zero-shear viscosity $\eta_0 = \eta_s + \eta_p$, the surface tension of the clear surface σ_0 , the capillary force σ_0/R and the maximum packing concentration of the surfactant Γ_∞ as the scales of length, time, viscosity, surface tension, pressure and surfactant concentration, respectively, the 1-D equations are non-dimensionalized as

$$\frac{\partial(S^2)}{\partial t} + \frac{\partial(S^2 u)}{\partial z} = 0, \tag{3.1}$$

$$\begin{aligned}
 \frac{\partial u}{\partial t} + u \frac{\partial u}{\partial z} &= \frac{3\beta Oh}{S^2} \frac{\partial \left(S^2 \frac{\partial u}{\partial z} \right)}{\partial z} + \frac{1}{S^2} \frac{\partial [S^2 (\tau_{zz} - \tau_{rr})]}{\partial z} \\
 & \quad - \frac{\partial}{\partial z} \left\{ C \left[\sigma + \frac{Oh(\kappa_s - \mu_s)}{S} \left(\frac{\partial(uS)}{\partial z} - \frac{C}{2} \frac{\partial(uS^2)}{\partial z} \right) \right] \right\} \\
 & \quad \text{①} \qquad \qquad \qquad \text{②} \\
 & \quad + \frac{2}{S} \left\{ \frac{\partial \sigma}{\partial z} + \frac{\partial}{\partial z} \left[\frac{Oh(\kappa_s - \mu_s)}{S} \left(\frac{\partial(uS)}{\partial z} - \frac{C}{2} \frac{\partial(uS^2)}{\partial z} \right) \right] \right\} \\
 & \quad \text{③} \qquad \qquad \qquad \text{④} \\
 & \quad + \frac{5Oh}{S^2} \frac{\partial}{\partial z} \left(\mu_s S \frac{\partial u}{\partial z} \right), \tag{3.2} \\
 & \quad \text{⑤}
 \end{aligned}$$

$$\tau_{zz} = \frac{(1-\beta)Oh}{De} \left(\frac{A_{zz}}{1 - \frac{tr(\mathbf{A})}{L^2}} - 1 \right), \tag{3.3}$$

$$\tau_{rr} = \frac{(1 - \beta)Oh}{De} \left(\frac{A_{rr}}{1 - \frac{tr(\mathbf{A})}{L^2}} - 1 \right), \tag{3.4}$$

$$De \left(\frac{\partial A_{zz}}{\partial t} + u \frac{\partial A_{zz}}{\partial z} - 2A_{zz} \frac{\partial u}{\partial z} \right) = 1 - \frac{A_{zz}}{1 - \frac{tr(\mathbf{A})}{L^2}}, \tag{3.5}$$

$$De \left(\frac{\partial A_{rr}}{\partial t} + u \frac{\partial A_{rr}}{\partial z} + A_{rr} \frac{\partial u}{\partial z} \right) = 1 - \frac{A_{rr}}{1 - \frac{tr(\mathbf{A})}{L^2}}, \tag{3.6}$$

$$\frac{\partial \Gamma}{\partial t} + \frac{1}{S} \frac{\partial (Su\Gamma)}{\partial z} - \frac{C\Gamma}{2S} \frac{\partial (S^2u)}{\partial z} = \frac{1}{Pe} \frac{1}{S} \frac{\partial \left(S \frac{\partial \Gamma}{\partial z} \right)}{\partial z}, \tag{3.7}$$

where

$$\kappa_s(\Gamma) = B_{\kappa\infty}\Gamma, \mu_s(\Gamma) = B_{\mu\infty}\Gamma, \sigma(\Gamma) = 1 + E \ln(1 - \Gamma), \tag{3.8}$$

$$C = \frac{1}{S \sqrt{1 + \left(\frac{\partial S}{\partial z} \right)^2}} - \frac{\frac{\partial^2 S}{\partial z^2}}{\left[1 + \left(\frac{\partial S}{\partial z} \right)^2 \right]^{3/2}}, \tag{3.9}$$

$$tr(\mathbf{A}) = A_{zz} + 2A_{rr}. \tag{3.10}$$

Note that the same symbols are used to denote both the dimensional and the dimensionless quantities for brevity. The dimensionless numbers appearing in the above 1-D equations are the Ohnesorge number $Oh = \eta_0 / \sqrt{\rho\sigma_0 R}$ representing the relative importance of bulk viscosity and capillarity, the solvent to solution viscosity ratio $\beta = \eta_s / \eta_0$, the Deborah number $De = \lambda_c / t_c$ measuring the relative importance of elasticity and capillarity, the surface Péclet number $Pe = R^2 / t_c D_s$ measuring the relative importance of surface convection and surface diffusion in surfactant transport, the elasticity number $E = R_g T \Gamma_\infty / \sigma_0$ measuring the activity of the surfactant or the sensitivity of the surface tension to changes in the surfactant concentration (in order to distinguish from the elasticity of the viscoelastic liquid, hereafter it is called the Marangoni number, as referred to in Ponce-Torres *et al.* 2016; Martínez-Calvo *et al.* 2020; Herrada *et al.* 2022) and the dilatational Boussinesq number $B_{\kappa\infty} = \kappa_s(\Gamma = \Gamma_\infty) / \eta_0 R = (\kappa_{sr} / \eta_0 R)(\Gamma_\infty / \Gamma_r)$ and the shear Boussinesq number $B_{\mu\infty} = \mu_s(\Gamma = \Gamma_\infty) / \eta_0 R = (\mu_{sr} / \eta_0 R)(\Gamma_\infty / \Gamma_r)$ measuring the relative importance of surface and bulk viscosities.

Equation (3.1) expresses the volume conservation, (3.2) is the 1-D momentum equation, (3.3)–(3.6) are the constitutive equations for the FENE-P viscoelastic model and (3.7) expresses the surfactant mass conservation. On the right-hand side of (3.2), the first term is the viscous force from the solvent, the second term is the viscoelastic force from the polymer and the rest of the terms, numbered ①–⑤, are all related to the surfactant, indicating that the surfactant influences the nonlinear dynamics of the viscoelastic thread in a complicated way. Specifically, term ① is the capillary force, term ③ is the Marangoni stress resulting from the spatial non-uniformity of the surface tension and terms ②, ④ and ⑤ are the surface viscous stresses associated with surface dilatational and shear deformations. If the surface dilatational viscosity κ_s is equal to the surface shear viscosity

μ_s , both term (2) and term (4) vanish and the momentum equation (3.2) is, fortunately, reduced. On the left-hand side of (3.7), the full curvature is preserved. If the slender body approximation is considered, (3.7) is simplified as

$$\frac{\partial(\Gamma^2)}{\partial t} + \frac{\partial(\Gamma^2 u)}{\partial z} = \frac{2}{Pe} \frac{\Gamma}{S} \frac{\partial}{\partial z} \left(S \frac{\partial \Gamma}{\partial z} \right). \quad (3.11)$$

When the finite extensibility L approaches infinity (polymer chains are infinitely extensible), the Oldroyd-B viscoelastic model is recovered, for which (3.1) and (3.2) and (3.7) remain unchanged, but the constitutive equations (3.3)–(3.6) reduce to

$$\tau_{zz} + De \left(\frac{\partial \tau_{zz}}{\partial t} + u \frac{\partial \tau_{zz}}{\partial z} - 2\tau_{zz} \frac{\partial u}{\partial z} \right) = 2(1 - \beta) Oh \frac{\partial u}{\partial z}, \quad (3.12)$$

$$\tau_{rr} + De \left(\frac{\partial \tau_{rr}}{\partial t} + u \frac{\partial \tau_{rr}}{\partial z} + \tau_{rr} \frac{\partial u}{\partial z} \right) = -(1 - \beta) Oh \frac{\partial u}{\partial z}. \quad (3.13)$$

If the Deborah number is set to be zero, the 1-D model reduces to that for Newtonian viscous liquid threads covered with insoluble surfactants, as proposed by Martínez-Calvo & Sevilla (2018) and Wee *et al.* (2021). In addition, if the surfactant concentration Γ is set to zero, the 1-D model reduces to that for surfactant-free viscoelastic threads of FENE-P type as built in Fontelos & Li (2004).

4. Numerical results

The 1-D equations (3.1)–(3.7) are solved by using an implicit finite difference scheme with adaptive mesh refinement (Li & He 2021). Considering both accuracy and efficiency, the number of spatial discrete points is 1000–1600, and the time step varies between 10^{-6} and 0.005. The convergence condition at each time step is that the maximum relative error is below 0.001. The calculation stops when the dimensionless minimum radius of the thread is less than 0.001. The validity of the code is checked by comparing with the results in Fontelos & Li (2004), Li & He (2021) and Wee *et al.* (2021).

At the initial time $t = 0$, the thread is perturbed by a small cosinusoidal harmonic disturbance, i.e.

$$S(z, t = 0) = \sqrt{1 - \frac{\epsilon_0^2}{2}} + \epsilon_0 \cos(kz), \quad (4.1)$$

where k is the dimensionless axial wavenumber and ϵ_0 is the initial amplitude of the disturbance whose value is fixed to 0.01.

Due to spatial periodicity and symmetry, only a half-wavelength long segment of the thread needs to be calculated. Therefore, in the calculation, the domain is limited to $z \in [0, \lambda/2]$, where $\lambda = 2\pi/k$ is the dimensionless wavelength of the disturbance.

The periodic boundary conditions are imposed at $z = 0$ and $z = \lambda/2$, i.e.

$$\left. \begin{aligned} \frac{\partial S}{\partial z}(z = 0, t) = \frac{\partial S}{\partial z}\left(z = \frac{\lambda}{2}, t\right) = 0, \quad u(z = 0, t) = u\left(z = \frac{\lambda}{2}, t\right) = 0, \\ \frac{\partial \tau_{zz}}{\partial z}(z = 0, t) = \frac{\partial \tau_{zz}}{\partial z}\left(z = \frac{\lambda}{2}, t\right) = 0, \quad \frac{\partial \tau_{rr}}{\partial z}(z = 0, t) = \frac{\partial \tau_{rr}}{\partial z}\left(z = \frac{\lambda}{2}, t\right) = 0, \\ \frac{\partial A_{zz}}{\partial z}(z = 0, t) = \frac{\partial A_{zz}}{\partial z}\left(z = \frac{\lambda}{2}, t\right) = 0, \quad \frac{\partial A_{rr}}{\partial z}(z = 0, t) = \frac{\partial A_{rr}}{\partial z}\left(z = \frac{\lambda}{2}, t\right) = 0, \\ \frac{\partial \Gamma}{\partial z}(z = 0, t) = \frac{\partial \Gamma}{\partial z}\left(z = \frac{\lambda}{2}, t\right) = 0. \end{aligned} \right\} \quad (4.2)$$

There are in total ten dimensionless parameters involved in this problem: Oh , β , De , L , Pe , E , $B_{\kappa\infty}$, $B_{\mu\infty}$, Γ_0 and k . The physical properties of surfactant-laden or viscoelastic fluids as well as the values of the dimensionless numbers considered in the literature are collected in [table 1](#). As one can see, the properties span a wide range. We would like to consider a viscoelastic thread of moderate viscosity and moderate elasticity. Suppose the density ρ is 1000 kg m^{-3} , the zero-shear viscosity η_0 is 0.1 Pa s , the stress relaxation time λ_c is 0.5 ms , the surface tension σ_0 is 0.05 N m^{-1} and the radius of the unperturbed thread R is $100 \text{ }\mu\text{m}$. Then, the Ohnesorge number Oh has a value of 1.4 and the Deborah number De has a value of 3.5 . The values of Oh and De are kept unchanged, since we focus on the effects of the surfactant on the dynamic behaviour of the viscoelastic thread. Without loss of generality, the solvent to solution viscosity ratio β is fixed to 0.5 and the finite extensibility parameter L takes a value of 5 for the FENE-P model. The surfactant surface diffusivity D_s is about 10^{-10} – $10^{-9} \text{ m}^2 \text{ s}^{-1}$ (Timmermans & Lister 2002; Martínez-Calvo & Sevilla 2018). The surface Péclet number Pe is of the order of magnitude of 10^3 to 10^6 , suggesting that surface convection is dominant in surfactant transport. In many studies, surface diffusion was reasonably neglected, i.e. the surface Péclet number was taken to be infinity (Timmermans & Lister 2002; Martínez-Calvo & Sevilla 2018; Alhushaybari & Uddin 2020; Martínez-Calvo *et al.* 2020; Wee *et al.* 2021). In addition to a case of large surface Péclet number ($Pe = 10^5$), we will examine a case of moderate surface Péclet number ($Pe = 1$), in which surface convection and surface diffusion are of equal importance. In small-scale applications such as microemulsions and nanoemulsions, the surface Péclet number can be order one ($O(1)$). We intend to discuss the effect of surfactant diffusivity on the nonlinear evolution of a viscoelastic thread via the moderate Pe case. The initial surfactant concentration Γ_0 varies between 0 and 0.5 . The range of the Marangoni number E is from 0 to 0.6 . The surface shear and dilatational viscosities are 10^{-5} – 10^{-4} Pa s m (Martínez-Calvo & Sevilla 2018) or much lower ($\sim 10^{-8} \text{ Pa s m}$) (Zell *et al.* 2014; Ponce-Torres *et al.* 2020). The Boussinesq numbers $B_{\kappa\infty}$ and $B_{\mu\infty}$ range widely from 0 to $O(10^3)$. The larger the Boussinesq numbers, the more important the surface viscous stresses. We consider a relatively conservative range of $B_{\kappa\infty}$ and $B_{\mu\infty}$ from 0 to 100 . Moreover, we assume that $B_{\kappa\infty}$ is equal to $B_{\mu\infty}$. The measurement of surface shear and dilatational viscosities is an experimental challenge. Some experiments showed that the surface dilatational viscosity can be orders of magnitude larger than the surface shear viscosity and can be augmented by adsorption if the surfactant is soluble (Lucassen & van den Tempel 1972; Alvarez *et al.* 2012; Singh & Narsimhan 2021, 2022; Herrada *et al.* 2022). The range of the axial wavenumber k is from 0.3 to 0.9 . All the values of the dimensionless numbers considered in the simulation are summarized in

ρ kg m ⁻³	η_b mPa s	η_0 mPa s	λ_c ms	σ_0 mN m ⁻¹	D_s m ² s ⁻¹	κ_s Pa s m	μ_s Pa s m	R mm	Oh	β	De	L	Pe	E	B_κ	B_μ	Papers
/	/	/	/	/	/	/	/	/	2, 4	0.5	10, 20	3, ∞	/	/	/	/	Fontelos & Li (2004)
/	1	1.37	12	60	/	/	/	[0.25, 5]	/	/	/	158	/	/	/	/	Wagner <i>et al.</i> (2005)
850	/	[72, 175]	[2.5, 11.5]	14.6	/	/	/	0.5	[1.13, 2.22]	[0.274, 0.67]	[1.15, 4.25]	[4.5, ∞]	/	/	/	/	Carroll & Ivo (2006)
1026	/	6.52×10^4	7.5×10^4	37	/	/	/	3	3.16	0.25	94.9	∞	/	/	/	/	Clasen <i>et al.</i> (2006a)
~ 1000	/	[3.4, 4.7]	[4.7, 8.2]	$O(10^{-2})$	/	/	/	2	$O(10^{-2})$	/	$O(10^{-3})$	$O(10^{-1})$	/	/	/	/	Tirtaamadja <i>et al.</i> (2006)
1000	1	3.7	0.17	60	/	/	/	0.14	0.04	0.27	0.8	∞	/	/	/	/	Ardekani <i>et al.</i> (2010)
1000	/	1	/	60	/	/	/	/	[0.01, 0.5]	≥ 0.5	[0.004, 0.5]	∞	/	/	/	/	Bhat <i>et al.</i> (2010)
1120	/	[14, 32]	[0.1, 19]	37	/	/	/	0.6	[0.09, 0.2]	/	[0, 0.47]	[15, ∞]	/	/	/	/	Tembley <i>et al.</i> (2012)
998	/	1.72	1.78	62.4	/	/	/	0.085	/	/	18.0	121	/	/	/	/	Mathues <i>et al.</i> (2018)
[1130, 1180]	/	[6, 22]	[0.045, 0.8]	[62, 66]	/	/	/	0.4	/	/	/	/	/	/	/	/	Sur & Rothstein (2018)
/	/	/	/	/	/	/	/	/	3.16	0.25	60	∞	/	/	/	/	Turkoz <i>et al.</i> (2018)
/	0.89	[2.2, 6200]	[0.22, 120]	/	/	/	/	0.635	[0.011, 31]	/	/	/	/	/	/	/	Dinic & Sharma (2020)
/	/	/	/	/	/	/	/	/	[0.1, 10]	/	/	/	[10 ⁻² , 10 ³]	[0, 1.5]	0	0	Dravid <i>et al.</i> (2006)
1260	/	1000	/	64	/	/	/	1.6	4.2	/	/	/	[0.1, 10 ⁵]	[0.3, 1]	0	0	Liao <i>et al.</i> (2006)
/	/	/	/	/	/	/	/	/	0.1	/	/	/	10 ⁴	0.3	0	0	McGough & Basaran (2006)
[985, 996]	/	[7.3, 276]	/	[38, 74]	~ 10 ⁻¹⁰	/	/	/	/	/	/	/	/	/	/	/	Dechelette <i>et al.</i> (2011)
/	/	/	/	/	/	/	/	/	0.01	/	/	/	[10 ⁴ , 10 ⁶]	[0, 1]	[0, 0.1] ⁰	[0, 0.1] ⁰	Ponce-Torres <i>et al.</i> (2016)
/	/	/	/	/	/	/	/	/	[0.82, 2.4]	[0.07, 0.188]	/	/	10 ³	[0.2, 0.4]	0	0	Kamat <i>et al.</i> (2018)
/	/	/	/	/	/	2.7 × 10 ⁻⁴	4 × 10 ⁻⁵	0.4	[0.1, 10]	/	/	/	∞	/	675 ⁰	100 ⁰	Martínez-Calvo & Sevilla (2018)
/	/	/	/	/	[10 ⁻⁹ , 10 ⁻⁸]	/	/	[0.001, 0.1]	[0.1, 10]	/	/	/	≥ 1	[0, 1]	≪ 1	≪ 1	Martínez-Calvo <i>et al.</i> (2020)
/	/	/	/	/	8 × 10 ⁻¹⁰	< 10 ⁻⁸	[10 ⁻⁹ , 10 ⁻⁷]	0.115	0.051	/	/	∞	7.73 × 10 ⁴	/	[0.0062, 0.62] ¹	< 0.062 ²	Ponce-Torres <i>et al.</i> (2020)
/	/	[1.7, 8.0]	[1.5, 3.4]	[38.6, 62.1]	/	/	/	0.635	/	/	/	/	/	/	/	/	Martínez-Narváez <i>et al.</i> (2021)
/	/	/	/	/	/	/	/	/	0.07	/	/	/	10 ³	0.3	0.0143 ⁰	0.0143 ⁰	Wee <i>et al.</i> (2021)
/	/	/	/	/	/	/	/	/	[0.32, ∞]	/	/	/	10 ³	0.2	[0, 10 ³] ⁰	[0, 1] ⁰	Herrada <i>et al.</i> (2022)

Table 1. The physical properties of surfactant-laden fluids and viscoelastic fluids and the values of the dimensional numbers in the literature. The superscripts 0 and c denote the Boussinesq numbers at Γ_0 and the CMC, respectively.

Dimensionless numbers	Values
the Ohnesorge number Oh	1.4
the solvent to solution viscosity ratio β	0.5
the Deborah number De	3.5
the finite extensibility parameter L	2, 5, 10, 50, ∞
the initial surfactant concentration Γ_0	0, 0.1, 0.2, 0.3, 0.5
the surface Péclet number Pe	$1, 10^5$
the Marangoni number E	0, 0.2, 0.4, 0.6
the dilatational Boussinesq number $B_{\kappa\infty}$	0, 0.1, 1, 10, 100
the shear Boussinesq number $B_{\mu\infty}$	0, 0.1, 1, 10, 100
the axial wavenumber k	0.3, 0.4, 0.5, 0.6, 0.7, 0.8, 0.9

Table 2. The values of the dimensionless numbers considered in the simulation.

table 2. Finally, to facilitate simulation and analysis, a reference state is selected, in which $Oh = 1.4$, $\beta = 0.5$, $De = 3.5$, $\Gamma_0 = 0.3$, $E = 0.4$, $Pe = 10^5$, $B_{\kappa\infty} = B_{\mu\infty} = 0$ and $L = 5$ (FENE-P) or ∞ (Oldroyd-B). The dimensionless numbers are fixed to the reference state unless specified otherwise.

4.1. Linear instability analysis based on the 1-D model

In this subsection, a brief linear analysis is performed based on the present 1-D model. Following the normal mode method, the quantities are decomposed into a base and a perturbation part, i.e.

$$(S, u, \tau_{zz}, \tau_{rr}, A_{zz}, A_{rr}, \Gamma) = \left(1, 0, 0, 0, \frac{L^2}{L^2 + 3}, \frac{L^2}{L^2 + 3}, \Gamma_0\right) + (\hat{S}, \hat{u}, \hat{\tau}_{zz}, \hat{\tau}_{rr}, \hat{A}_{zz}, \hat{A}_{rr}, \hat{\Gamma}) \exp(\alpha t + jkz) + \text{c.c.}, \quad (4.3)$$

where the hat denotes the initial amplitudes of the perturbation parts, α is the complex frequency with the real part α_r the temporal growth rate and the imaginary part α_i the speed of wave propagation, j is the imaginary unit and ‘c.c.’ denotes the complex conjugate.

Linearizing the 1-D equations (3.1)–(3.7) and then substituting the decomposition (4.3) into the linearized equations, we obtain a set of linear homogeneous algebraic equations for the unknowns $(\hat{S}, \hat{u}, \hat{\tau}_{zz}, \hat{\tau}_{rr}, \hat{A}_{zz}, \hat{A}_{rr}, \hat{\Gamma})$. The determinant of the coefficient matrix of the equations has to be zero to ensure the system has non-trivial solutions, which yields the following dispersion relation:

$$\alpha + 3\beta Ohk^2 = -k^2(1 - \beta)Oh \frac{L^2 + 3}{L^2} (\mathcal{E}_1 - \mathcal{E}_2) - \frac{k^2 E \Gamma_0}{2(1 - \Gamma_0) \left(\alpha + \frac{k^2}{Pe}\right)} + \frac{\sigma_i k^2 (1 - k^2)}{2\alpha} - \frac{B_{\kappa\infty} + 9B_{\mu\infty}}{2} \Gamma_0 Ohk^2, \quad (4.4)$$

where

$$\mathcal{E}_1 = \frac{\begin{vmatrix} \frac{2L^2}{L^2+3} & \frac{2(L^2+3)}{L^4} \\ -\frac{L^2}{L^2+3} & De\alpha + \frac{L^2+3}{L^2} + \frac{2(L^2+3)}{L^4} \end{vmatrix}}{\begin{vmatrix} De\alpha + \frac{L^2+3}{L^2} + \frac{L^2+3}{L^4} & \frac{2(L^2+3)}{L^4} \\ \frac{L^2}{L^2+3} & De\alpha + \frac{L^2+3}{L^2} + \frac{2(L^2+3)}{L^4} \end{vmatrix}}, \quad (4.5)$$

$$\mathcal{E}_2 = \frac{\begin{vmatrix} De\alpha + \frac{L^2+3}{L^2} + \frac{L^2+3}{L^4} & \frac{2L^2}{L^2+3} \\ \frac{L^2}{L^2+3} & -\frac{L^2}{L^2+3} \end{vmatrix}}{\begin{vmatrix} De\alpha + \frac{L^2+3}{L^2} + \frac{L^2+3}{L^4} & \frac{2(L^2+3)}{L^4} \\ \frac{L^2}{L^2+3} & De\alpha + \frac{L^2+3}{L^2} + \frac{2(L^2+3)}{L^4} \end{vmatrix}}, \quad (4.6)$$

and $\sigma_i (= 1 + E \ln(1 - \Gamma_0))$ is the initial surface tension corresponding to the initial surfactant concentration Γ_0 . Note that the four terms on the right-hand side of (4.4) are related to the viscoelasticity of the polymer solution, the Marangoni stress, the surface tension and the surface shear and dilatational viscosities, respectively.

When the finite extensibility L approaches infinity, the dispersion relation (4.4) reduces to that for the linear Jeffreys model and any nonlinear viscoelastic model (e.g. Oldroyd-B and FENE-P) that becomes the Jeffreys model after linearization, i.e.

$$\begin{aligned} \alpha + 3\beta Ohk^2 = & -\frac{3k^2(1-\beta)Oh}{1+De\alpha} - \frac{k^2E\Gamma_0}{2(1-\Gamma_0)\left(\alpha + \frac{k^2}{Pe}\right)} \\ & + \frac{\sigma_i k^2(1-k^2)}{2\alpha} - \frac{B_{\kappa\infty} + 9B_{\mu\infty}}{2}\Gamma_0 Ohk^2. \end{aligned} \quad (4.7)$$

When the Deborah number De is equal to zero, (4.7) reduces to the dispersion relation determining the linear instability characteristics of surfactant-laden Newtonian viscous threads (Martínez-Calvo & Sevilla 2018), i.e.

$$\alpha + 3Ohk^2 = -\frac{k^2E\Gamma_0}{2(1-\Gamma_0)\left(\alpha + \frac{k^2}{Pe}\right)} + \frac{\sigma_i k^2(1-k^2)}{2\alpha} - \frac{B_{\kappa\infty} + 9B_{\mu\infty}}{2}\Gamma_0 Ohk^2. \quad (4.8)$$

The effect of the dimensionless numbers on the linear instability of the surfactant-covered viscoelastic thread is shown in figure 2. It can be seen that the temporal growth rate α_r decreases with the increase in the initial surfactant concentration Γ_0 , the surface Péclet number Pe , the Marangoni number E , the dilatational Boussinesq number $B_{\kappa\infty}$ or the shear Boussinesq number $B_{\mu\infty}$ (see figures 2a–2f). In general, surfactants suppress the linear instability of viscoelastic threads, as they affect Newtonian viscous threads (Hansen *et al.* 1999; Timmermans & Lister 2002; Martínez-Calvo & Sevilla 2018). The mechanism can be interpreted from several aspects: the presence of the surfactant

lowers the surface tension and thereby the capillary force that destabilizes the viscoelastic thread; the Marangoni stress tends to eliminate the spatial non-uniformity of the surface tension and thereby suppresses the growth of the disturbance; the surface shear and dilatational viscosities and the resulting viscous stresses have a stabilizing effect on the viscoelastic thread.

Comparing the large Pe case in [figure 2\(a\)](#) with the moderate Pe case in [figure 2\(b\)](#), the temporal growth rate α_r is apparently more sensitive to the presence of the surfactant at larger values of Pe . Recall that the surface Péclet number Pe represents the relative importance of surface convection and surface diffusion in surfactant transport. At large values of Pe , surface convection is dominant, resulting in high non-uniformity of surfactant and thereby large Marangoni stress that suppresses the instability of the thread. This trend can also be seen in [figure 2\(c\)](#). The cutoff wavenumber k_c , beyond which the thread is linearly stable ($\alpha_r \leq 0$), remains at unity no more in the presence of the surfactant. Analytically the cutoff wavenumber k_c can be obtained from the dispersion relation (4.4). Setting the complex frequency α in (4.4) to be zero, we have

$$k_c = \sqrt{1 - \frac{E\Gamma_0}{\sigma_i(1 - \Gamma_0)}}. \quad (4.9)$$

Clearly, k_c is strictly equal to unity only when Γ_0 is zero. As shown in [figure 2](#), k_c decreases (that is, the range of unstable axial wavenumbers is narrowed down) as Γ_0 , Pe or E increases. However, this statement may not be true since the high-order terms are neglected in the 1-D model, as pointed out by Hansen *et al.* (1999), Timmermans & Lister (2002) and Martínez-Calvo & Sevilla (2018) in the study of Newtonian threads. The 2-D axisymmetric linear instability analysis has showed that the cutoff wavenumber remains at unity. The 1-D model may overestimate the suppressing effect of the surfactant on the thread instability at large wavenumbers near the cutoff. To eliminate the discrepancy, necessary high-order terms should be retained in the long wave approximation (Martínez-Calvo & Sevilla 2018), which is of interest but beyond the scope of the present research. Anyway, the 1-D model does not need to give results that agree with the 2-D instability analysis over the entire unstable wavenumber range. We can still get some insights into how surfactants affect the linear instability and nonlinear behaviour of viscoelastic threads via the 1-D model.

A non-Newtonian viscoelastic thread possesses a higher temporal growth rate than its Newtonian viscous counterpart. That is, elasticity has a destabilizing effect on the linear instability of a thread (Brenn *et al.* 2000). It is found that finite extensibility affects viscoelastic threads in a different way. As shown in [figure 2\(g\)](#), the temporal growth rate α_r increases as the finite extensibility parameter L decreases, suggesting that the extensibility of polymer chains suppresses the instability of the thread.

4.2. Nonlinear behaviour of a surfactant-covered Oldroyd-B viscoelastic thread

An Oldroyd-B viscoelastic liquid thread never breaks up because of its infinite extensibility. The 1-D models, the 2-D axisymmetric numerical simulations and the experiments have shown that a quasistatic beads-on-a-string structure is gradually formed during the nonlinear evolution of an Oldroyd-B viscoelastic thread (Chang *et al.* 1999; Ardekani *et al.* 2010; Tembely *et al.* 2012; Turkoz *et al.* 2018). Moreover, the filament between two adjacent primary droplets, with an almost uniform thickness, thins exponentially in time at a rate of $1/3De$, and the flow in the filament is uniaxial extensional (Clasen *et al.* 2006a). The influence of other factors such as electric field, temperature, surfactant and exterior fluid phase on the dynamics of viscoelastic jets and threads has

Dynamics of surfactant-covered viscoelastic threads

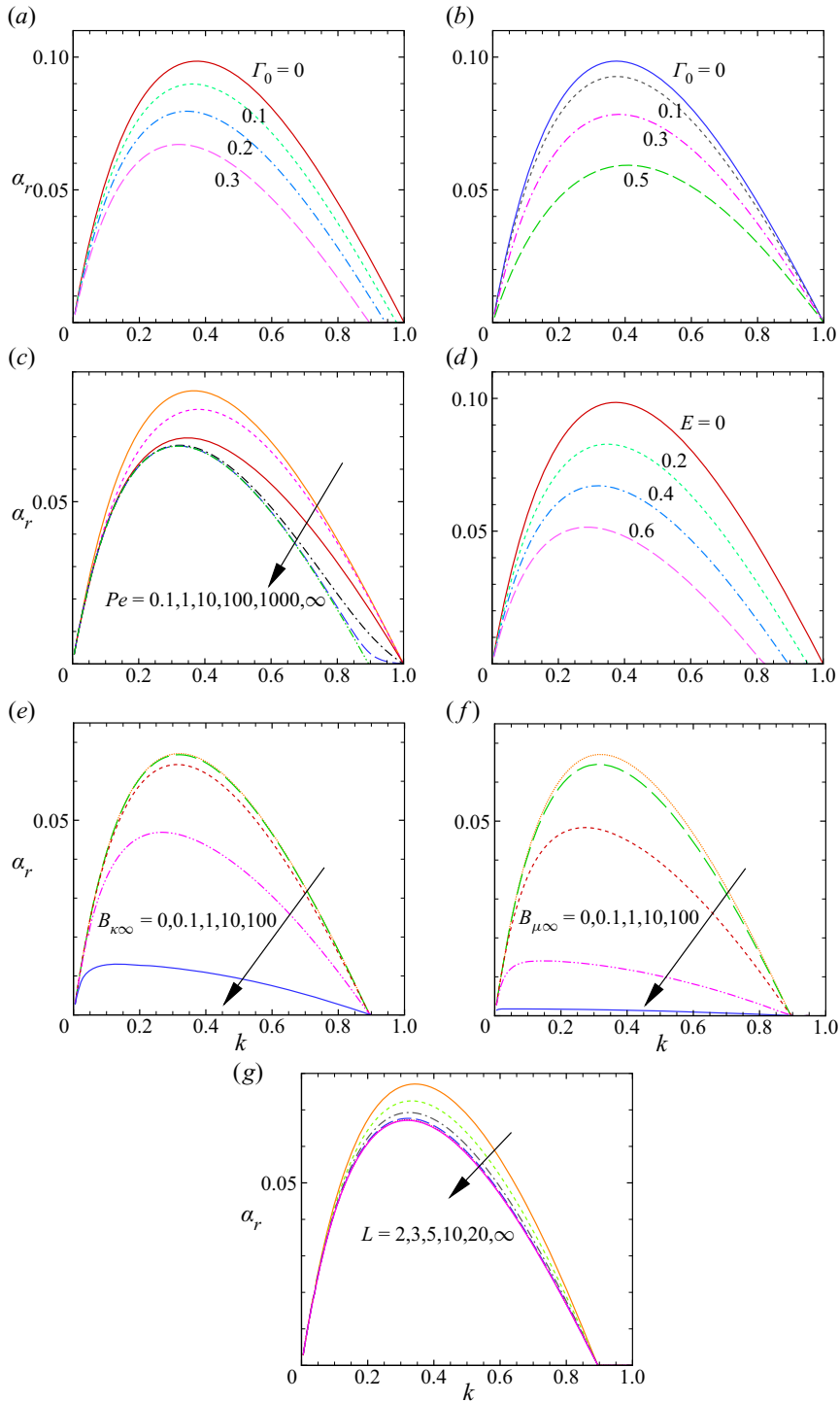


Figure 2. The temporal growth rate α_r vs the axial wavenumber k . The effect of (a–b) the initial surfactant concentration Γ_0 , (c) the surface Péclet number Pe , (d) the Marangoni number E , (e) the dilatational Boussinesq number $B_{k\infty}$, (f) the shear Boussinesq number $B_{\mu\infty}$ and (g) the finite extensibility parameter L . In (a), $Pe = 10^5$; in (b), $Pe = 1$. (a–f) The Oldroyd-B model ($L \rightarrow \infty$) and (g) the FENE-P model. The arrows denote the direction of a parameter increasing.

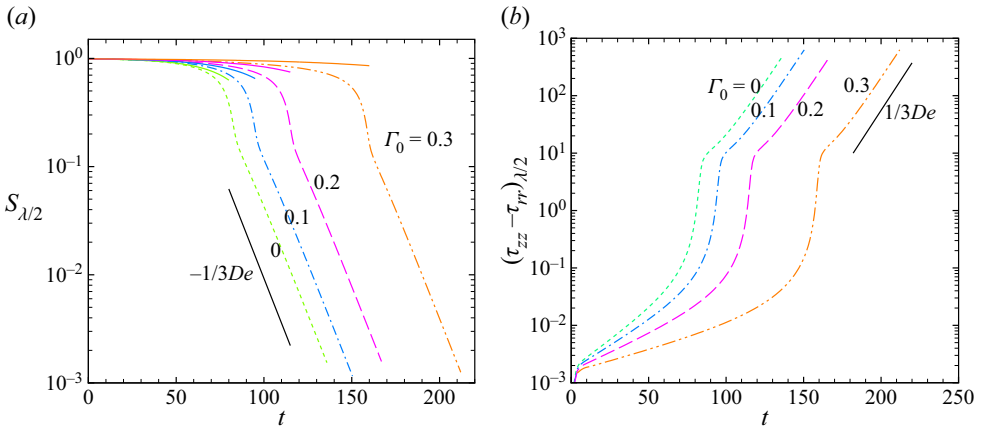


Figure 3. Effect of the initial surfactant concentration Γ_0 on the thinning of the Oldroyd-B viscoelastic thread. (a) The thread radius S and (b) the first normal stress difference $\tau_{zz} - \tau_{rr}$ at the midpoint $z = \lambda/2$. Here, $k = 0.8$. The solid lines in (a) are the predictions of linear theory.

drawn attention in recent years (Eggers & Villiermaux 2008; Montanero & Gañán-Calvo 2020). In the following, we examine how the presence of a surfactant monolayer affects the nonlinear behaviour of an Oldroyd-B viscoelastic thread.

The effect of the initial surfactant concentration Γ_0 on the temporal evolution of the Oldroyd-B viscoelastic thread is shown in figure 3, where the large surface Péclet number case ($Pe = 10^5$) is considered and the surface dilatational and shear viscosities are turned off ($B_{k\infty} = B_{\mu\infty} = 0$). As shown in figure 3(a), the radius of the Oldroyd-B viscoelastic thread at the midpoint $z = \lambda/2$ (where the centre of the filament is located), denoted by $S_{\lambda/2}$, first experiences a fast decrease and then enters a slow exponential thinning, regardless of the presence of the surfactant. The surfactant has a negligible influence on the $1/3De$ exponential thinning law of the filament. A local balance between the capillary and elastic forces is presumably established in the filament as in the absence of the surfactant. The first normal stress difference $\tau_{zz} - \tau_{rr}$ increases exponentially in time at the rate $1/3De$, as shown in figure 3(b). It indicates that the surfactant plays a minimal role at the late stages of filament thinning. In contrast, the surfactant does greatly influence the evolution of the thread at the early stages. Most notably, the decrease of $S_{\lambda/2}$ is slowed down in the presence of the surfactant. As shown in figure 3(a), the filament needs increasingly more time to reach the uniaxial extension stage, as Γ_0 increases. This trend is qualitatively in accordance with the linear prediction in figure 2(a). The temporal evolution of $S_{\lambda/2}$ predicted by linear theory is included in figure 3(a) for comparison (the solid lines). The 1-D linear theory turns out to underestimate the development of the disturbance as the nonlinear effects come into play.

To understand the negligible effect of the surfactant on the thinning of the viscoelastic thread at the late stages, the variation of the thread radius S , the surfactant concentration Γ , the surface tension σ , the axial velocity u and the first normal stress difference $\tau_{zz} - \tau_{rr}$ along the thread are examined in figure 4(a) for the large surface Péclet number case ($Pe = 10^5$) and the initial surfactant concentration $\Gamma_0 = 0.3$ (the reference state). Obviously, at the observed time $t = 212$, the beads-on-a-string structure has been formed and an elasto-capillary balance has been established inside the filament. Note that the surfactant concentration Γ varies along the thread in a way quite similar to the thread radius S . As a matter of fact, at a value of the surface Péclet number as large as 10^5 , the

diffusion term on the right-hand side of the surfactant advection–diffusion equation (3.7) or (3.11) is very small. Neglecting the diffusion term, (3.8) approximates to

$$\frac{\partial(\Gamma^2)}{\partial t} + \frac{\partial(\Gamma^2 u)}{\partial z} = 0. \tag{4.10}$$

The above equation is the same in form with the volume conservation equation (3.1), implying that the spatio-temporal evolution of the surfactant concentration Γ and the thread radius S follows the same discipline. Hence, we can write

$$\Gamma(z, t) = aS(z, t), \tag{4.11}$$

where a is a coefficient to be determined. Apparently, $a = \Gamma_0$. The surface tension σ in figure 4(a) is approximated as

$$\sigma = 1 + E \ln(1 - \Gamma_0 S). \tag{4.12}$$

Most of surfactant molecules initially residing at the filament surface have been convected to the primary droplet before the thread enters the final elasto-capillary stage, due to the strong convection. The filament is almost free of surfactant in the elasto-capillary regime, with a nearly zero Γ and a nearly unity σ . Due to the evacuation of the surfactant, the $1/3De$ exponential thinning law is maintained, the axial velocity u goes linearly with z and the first normal stress difference $\tau_{zz} - \tau_{rr}$ is spatially uniform in the filament, as illustrated in figure 4(a).

For a viscoelastic thread with no surfactant, the shape of primary droplets is almost spherical under the action of surface tension (Clasen *et al.* 2006a). If the viscosity is small, primary droplets undergo shape oscillations until energy is dissipated (Ardekani *et al.* 2010; Li, Yin & Yin 2017). For the moderate viscosity considered in this problem, no oscillation takes place. On the other hand, the presence of the surfactant is found to alter the beads-on-a-string morphology to some extent. In figures 5(a) and 5(b), the thread profiles are plotted for different values of the initial surfactant concentration Γ_0 and a fixed value of the axial wavenumber $k = 0.5$. It is shown that the surfactant leads to the stretch of the primary droplets in the axial direction. The primary droplets are spherical no more. They look like prolate spheroids in shape. Moreover, they deform more and more as the initial surfactant concentration Γ_0 increases. The deformation may be caused by the Marangoni stress that tends to drive liquid from the small surface tension region (the primary droplets) to the large surface tension region (the filament).

There is a secondary droplet between two adjacent primary ones, located at the midpoint $z = \lambda/2$. Increasing the surfactant concentration results in the decrease in the secondary droplet size, as illustrated in figure 5(b). The volume of the secondary droplet, denoted by V_s , is shown in figure 5(c). Clearly, V_s decreases as the initial surfactant concentration Γ_0 increases. When Γ_0 is large enough, the secondary droplet can be completely removed. For instance, for the axial wavenumber $k = 0.7$, the secondary droplet disappears at a value of Γ_0 as large as 0.3. The calculation result shows that the secondary droplet begins to form at the late stages of filament thinning. The mechanism, responsible for the decrease in secondary droplet size, might lie in that the tiny amount of surfactant at the filament surface slightly weakens the local capillary force and thereby impedes the formation of secondary droplet. In figure 8 below, it is shown that the Marangoni stress also plays a role in reducing the secondary droplet size. In applications, surfactants may help eliminate unwelcome secondary droplets arising in viscoelastic threads, as long as surface convection is strong enough. It is also shown in figure 5(c) that the volume of the secondary droplet increases as the axial wavenumber k decreases. The most unstable

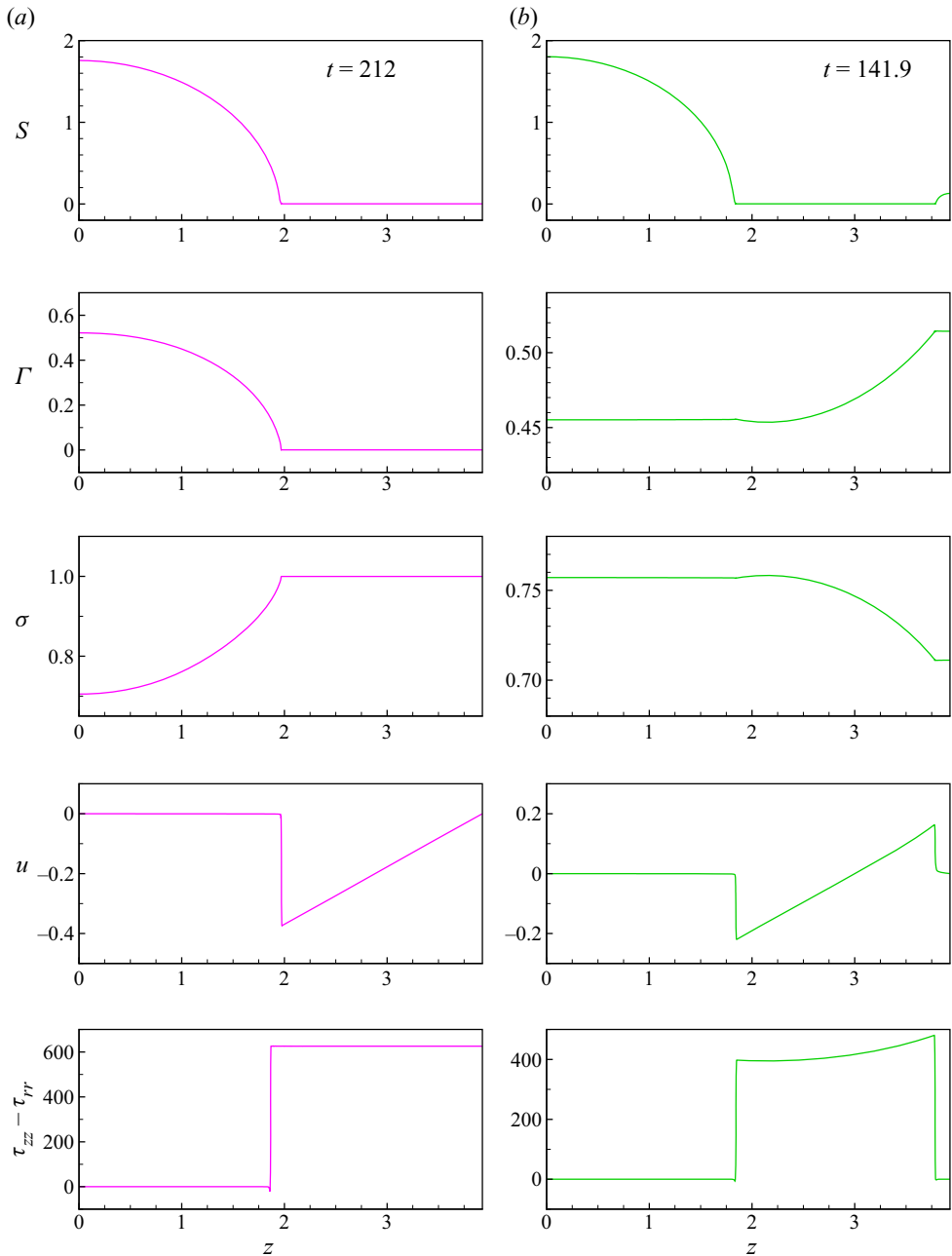


Figure 4. Variation of the thread radius S , the surfactant concentration Γ , the surface tension σ , the axial velocity u and the first normal stress difference $\tau_{zz} - \tau_{rr}$ along the thread. In panel (a), $Pe = 10^5$; in panel (b), $Pe = 1$. Here, $k = 0.8$.

wavenumber k_{max} corresponding to the maximum growth rate is most probably dominant in nature. According to the 1-D linear result in figure 2(a), the most unstable wavenumber is generally small. For $\Gamma_0 = 0$, $k_{max} = 0.375$; as Γ_0 increases, k_{max} decreases. On the other hand, the tendency in figure 5(c) suggests that the nonlinear evolution of the viscoelastic

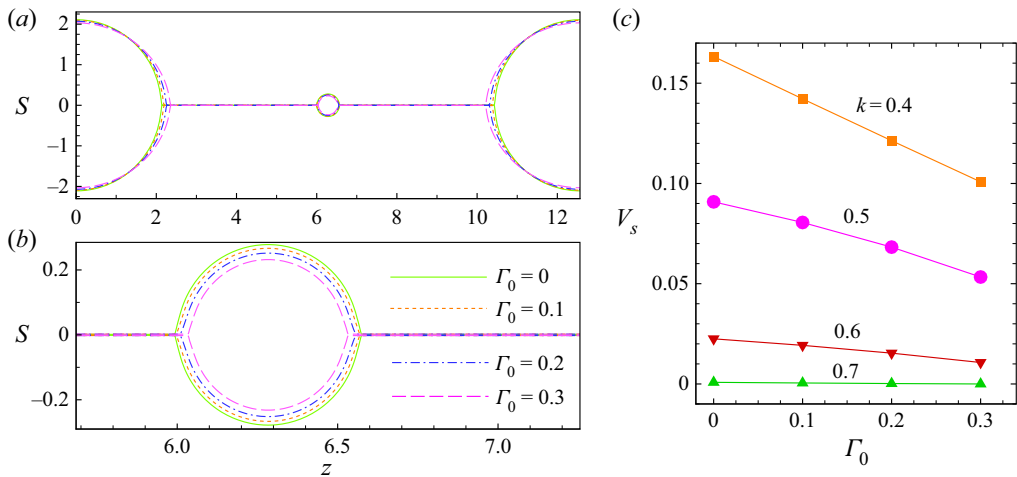


Figure 5. (a) Thread profiles for different values of the initial surfactant concentration Γ_0 , where $k = 0.5$. (b) Zoomed-in secondary droplets located at the midpoint $z = \lambda/2$, where $t = 100.85$ ($\Gamma_0 = 0$), 100.55 ($\Gamma_0 = 0.1$), 105.1 ($\Gamma_0 = 0.2$) and 113.9 ($\Gamma_0 = 0.3$). (c) Dependence of the secondary droplet volume V_s on Γ_0 and k .

thread exposed to natural disturbances yields secondary droplets of large volume, at least larger than those for $k = 0.4$.

The moderate surface Péclet number case is examined in figure 6. At $Pe = 1$, surface diffusion is comparable to surface convection and the motion of the surfactant is governed by both factors. The temporal evolution of the thread radius at the midpoint, $S_{\lambda/2}$, is illustrated in figure 6(a) for different values of the initial surfactant concentration Γ_0 and a fixed axial wavenumber $k = 0.9$. For a small value of Γ_0 equal to 0.1, $S_{\lambda/2}$ decreases all the way and the thread evolves into a beads-on-a-string structure with no secondary droplet. At the large times the thinning of the filament is little influenced by the surfactant and basically follows the $1/3De$ exponential law in time. The scenario is changed with Γ_0 increasing, see the lines for $\Gamma_0=0.3$ and 0.5 in figure 6(a). At some instant, $S_{\lambda/2}$ begins to go upward, indicating that a secondary droplet is formed at the midpoint. Moreover, the size of the secondary droplet increases as Γ_0 increases. The predictions of linear theory are shown in figure 6(a) (the solid lines) for comparison.

The spatio-temporal evolution of the surfactant concentration Γ and the surface tension σ is illustrated in figures 6(b)–6(e) for the large Pe case and the moderate Pe case, respectively, where the initial surfactant concentration Γ_0 is fixed to 0.3. Compared with the large Pe case, in the moderate Pe case the surfactant layer remains almost equally dense over the entire thread due to the surface diffusion mechanism. Recall that the surface area of the thread tends to decrease all the way to minimize the surface energy. Reasonably, the surfactant concentration Γ increases monotonically with time from its initial value Γ_0 , and the surface tension σ decreases monotonically. Due to its abundance and non-uniform distribution at the filament surface, the surfactant affects significantly the thinning characteristics of the filament. An elasto-capillary balance fails to be established within the filament. Under the action of the capillary force and possibly the Marangoni stress as well, a small quantity of liquid is driven towards the midpoint $z = \lambda/2$ and forms a secondary droplet there.

For the case of moderate surface Péclet number $Pe = 1$, the thread profiles are plotted in figure 7 for different values of the initial surfactant concentration Γ_0 and the axial wavenumber $k = 0.5$. Most interestingly, the secondary droplet at the midpoint gains

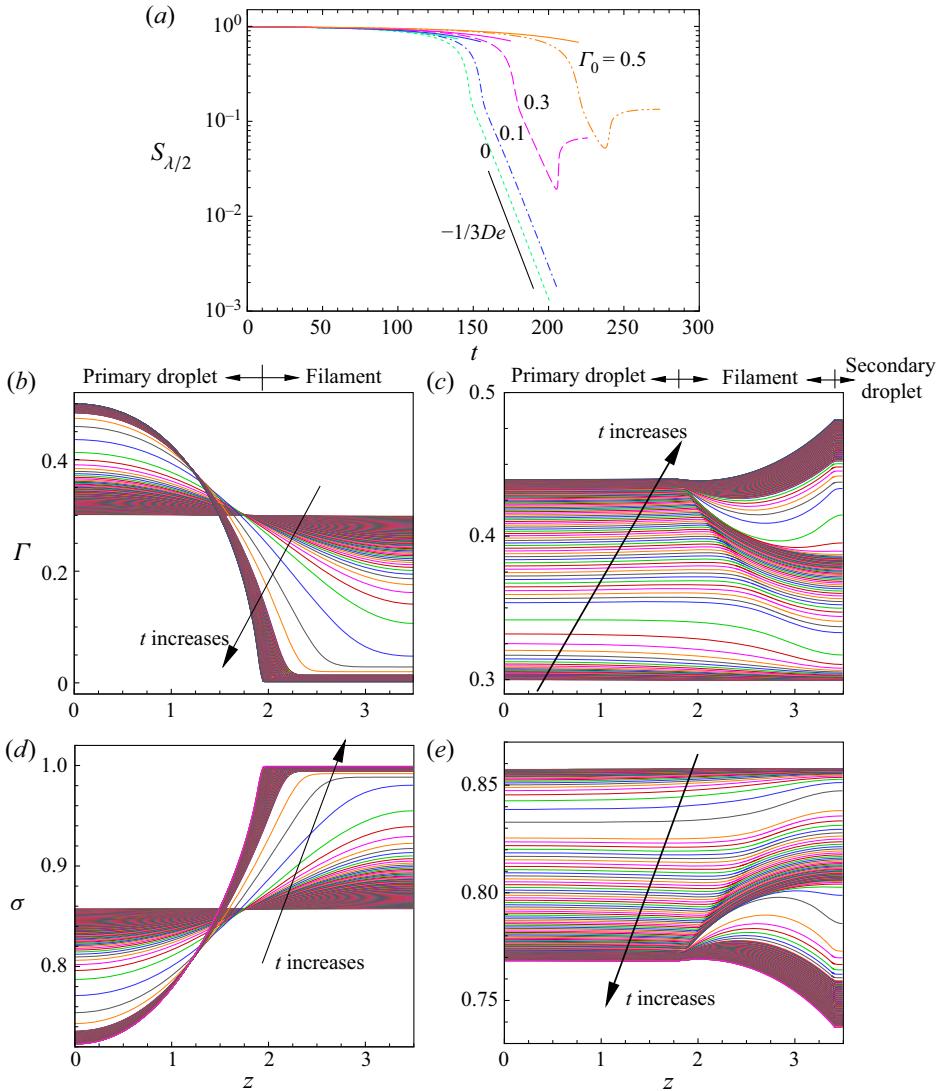


Figure 6. (a) Effect of the initial surfactant concentration Γ_0 on the temporal evolution of the thread radius at the midpoint, $S_{\lambda/2}$, where $Pe = 1$ and the solid lines are the predictions of linear theory. Spatial distribution of (b,c) the surfactant concentration Γ and (d,e) the surface tension σ along the thread as time increases, where $\Gamma_0 = 0.3$. In (b) and (d), $Pe = 10^5$; in (c) and (e), $Pe = 1$. Here, $k = 0.9$.

weight as Γ_0 increases. This trend is opposite to the large Pe case shown in figure 5. In addition, high-order secondary droplets appear in the filament when Γ_0 is sufficiently large, see the profile for $\Gamma_0 = 0.5$.

The effect of the Marangoni stress is explored in figure 8 by comparing the case in which the Marangoni stress is taken into account with the case in which it is turned off. Figure 8(a) illustrates the temporal evolution of the thread radius at the midpoint, $S_{\lambda/2}$, for the axial wavenumbers $k = 0.8$ and 0.9 . For such large axial wavenumbers, no secondary droplet is formed in the beads-on-a-string structure. It can be seen that the Marangoni stress slows down the growth of the disturbance and delays the arrival of the

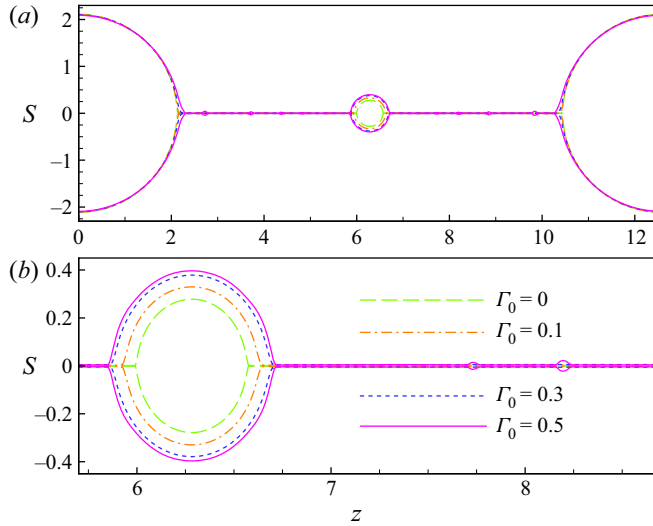


Figure 7. The case of moderate surface Péclet number $Pe = 1$. (a) Thread profiles for different values of the initial surfactant concentration Γ_0 and (b) zoomed-in secondary droplets at the midpoint $z = \lambda/2$. Here, $k = 0.5$ and $t = 100.85$ ($\Gamma_0 = 0$), 95.75 ($\Gamma_0 = 0.1$), 99.4 ($\Gamma_0 = 0.3$) and 122.3 ($\Gamma_0 = 0.5$).

elasto-capillary stage to a great extent. That is, the Marangoni stress acts as a resistance to the instability of the viscoelastic thread. On the other hand, the Marangoni stress has no significant effect on the exponential thinning law of the filament in the elasto-capillary regime (recall that this is the case of large surface Péclet number). The effect of the Marangoni stress on the thread profile is examined in figures 8(b) and 8(c). For small axial wavenumbers such as $k = 0.5$ and 0.6 , a secondary droplet unavoidably appears at the midpoint of the filament. The Marangoni stress decreases the size of the secondary droplet to a certain extent. In addition, the Marangoni stress stretches the primary droplets in the axial direction and makes them more prolate, as illustrated previously in figure 5.

The primary droplets attain an almost static shape in the elasto-capillary regime. It is of interest to seek the static solution to the shape of primary droplets. For a surfactant-free viscoelastic thread, the static solution is a sphere (Clasen *et al.* 2006a), as illustrated in figure 9(a). When the thread is covered with a surfactant monolayer, its primary droplets are spherical no more. The static solution can be readily obtained in some simplified cases. For instance, if we neglect the time-dependent term, the inertia, the viscoelastic stress and the surface shear and dilatational viscosities (in the primary droplet region this simplification is reasonable), the momentum equation (3.2) yields

$$\frac{\partial(\sigma C)}{\partial z} - \frac{2}{S} \frac{\partial \sigma}{\partial z} = 0. \tag{4.13}$$

In the large surface Péclet number case, the surface tension σ can be approximated by (4.12). The substitution of (4.12) into (4.13) yields

$$\frac{\partial(\sigma C)}{\partial z} + \frac{2E\Gamma_0}{S(1 - \Gamma_0 S)} \frac{\partial S}{\partial z} = 0. \tag{4.14}$$

Note that both σ and C are functions of $S(z)$ only. So (4.14) is essentially an ordinary differential equation for S

$$\frac{\partial}{\partial z} [\sigma C + 4E\Gamma_0 \arctan(2\Gamma_0 S - 1)] = 0. \tag{4.15}$$

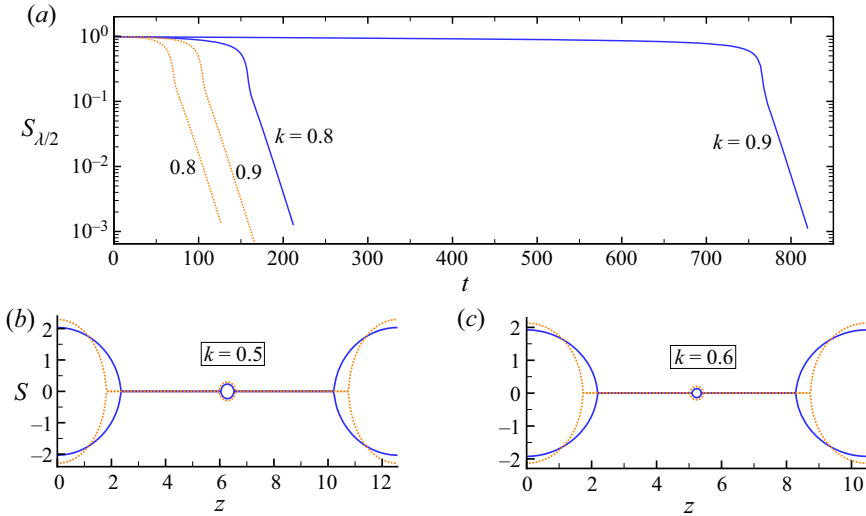


Figure 8. Effect of the Marangoni stress. (a) Temporal evolution of the thread radius at the midpoint, $S_{\lambda/2}$, for $k = 0.8$ and 0.9 ; (b) and (c) thread profiles for $k = 0.5$ and 0.6 , respectively. Solid lines: the Marangoni stress is taken into account; dotted lines: the Marangoni stress is turned off. In (b), $t = 113.9$ (Marangoni) and 92 (no Marangoni); in (c), $t = 126.85$ (Marangoni) and 104.6 (no Marangoni).

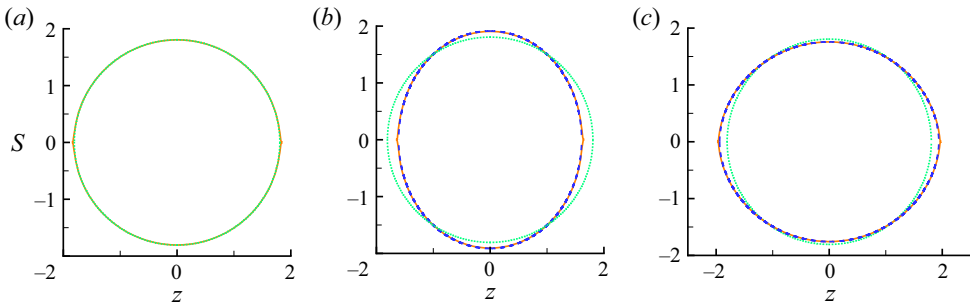


Figure 9. Shape of the primary droplet located at the origin $z = 0$. The cases of (a) a surfactant-free viscoelastic thread, (b) a surfactant-covered viscoelastic thread with the Marangoni stress turned off and (c) a surfactant-covered viscoelastic thread with the Marangoni stress taken into account. The dotted lines denote an isolated spherical droplet of the same volume. The solid lines denote the primary droplets simulated by the 1-D model. The dashed lines denote the static solutions. Here, $k = 0.8$.

An analytical solution to (4.14) or (4.15) may exist or not. We turn to numerical methods such as finite difference.

A static solution is plotted in figure 9(c). It is shown that the static solution agrees well with the 1-D numerical simulation. As outlined previously, the primary droplet exhibits a prolate spheroid profile under the action of the Marangoni stress. In contrast, when the Marangoni stress is turned off, the primary droplet becomes oblate, as illustrated in figure 9(b). That is, the primary droplet is stretched in the radial direction, due to the spatial non-uniformity of the surface tension.

The effect of the Marangoni number E on the nonlinear evolution of the Oldroyd-B viscoelastic thread is shown in figure 10. As shown in figure 10(a), the Marangoni number E prolongs the early stages of thread thinning. As the Marangoni number increases, the local capillary force decreases and the Marangoni stress increases. Both factors result

Dynamics of surfactant-covered viscoelastic threads

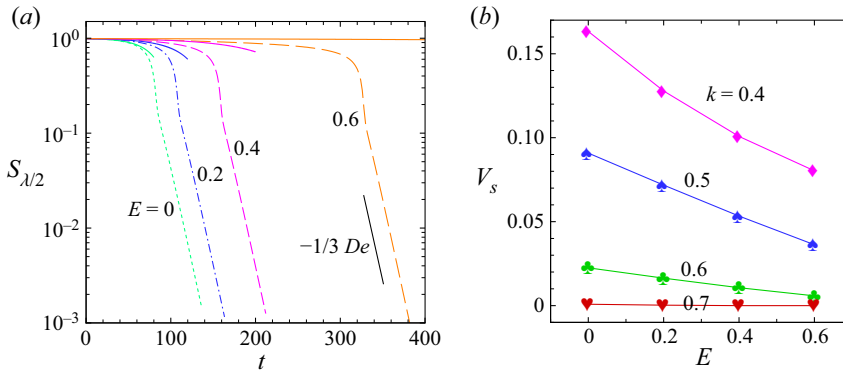


Figure 10. Effect of the Marangoni number E on the nonlinear behaviour of the Oldroyd-B viscoelastic thread. (a) Temporal evolution of the thread radius at the midpoint, $S_{\lambda/2}$, where $k = 0.8$ and the solid lines are the predictions of linear theory. (b) Dependence of the secondary droplet volume V_s on E and k . Note that for $k = 0.7$ and $E = 0.4$ or 0.6 the secondary droplet actually does not exist.

in the decrease in the temporal growth rate of the initial disturbance, as predicted by linear theory. At the final stage, an elasto-capillary balance is established in the filament and the $1/3De$ exponential law is little influenced by the Marangoni number (recall that this is the large surface Péclet number case). On the other hand, the Marangoni number influences the beads-on-a-string morphology. Particularly, it decreases the size of the secondary droplet or even leads to the disappearance of the secondary droplet, as illustrated in figure 10(b). The capillary force at the filament surface decreases as the Marangoni number increases. This tendency might be responsible for the weight loss of the secondary droplet. The 1-D linear result in figure 2(d) shows that the most unstable wavenumber k_{max} decreases from 0.375 as the Marangoni number E increases from zero. Figure 10(b) shows that the smaller the axial wavenumber, the larger the secondary droplet. So secondary droplets formed under natural excitations are predicted to possess volumes larger than those for $k = 0.4$ in figure 10(b).

The measurement of surface shear and dilatational viscosities is technically challenging due to the difficulty of separating the surface rheological effects from the Marangoni effects (Kamat *et al.* 2018; Wee *et al.* 2020). Several recent analytical and numerical studies on Newtonian threads have accounted for the surface viscosities and proposed possible routes to measuring the surface rheological properties (Wee *et al.* 2020, 2021). The effect of the surface viscosities on Newtonian threads are summarized in table 3. In the following, we examine their effect on the nonlinear dynamics of Oldroyd-B viscoelastic threads.

Figure 11 illustrates the temporal evolution of the thread radius S , the first normal stress difference $\tau_{zz} - \tau_{rr}$, the extension rate $\dot{\epsilon} (= \partial u / \partial z)$ and the Trouton ratio $\eta_E / \eta_0 (= 3\beta + (\tau_{zz} - \tau_{rr}) / Oh\dot{\epsilon})$, η_E : the elongational viscosity) at the midpoint $z = \lambda/2$ for the axial wavenumber $k = 0.8$, where a wide range of the Boussinesq numbers is considered. It is shown that the thinning of the viscoelastic thread can be delayed to an extraordinary extent at large values of the Boussinesq numbers, in agreement with the tendency predicted by linear theory in figures 2(e) and 2(f).

At large values of the Boussinesq numbers such as 10 and 100, the final stage of filament thinning is characterized by a uniaxial extensional flow no more. If the flow were uniaxial extensional, the extension rate $\dot{\epsilon}$ would approach the constant $2/3De$. However, as shown in figure 11(c), for $B_{\kappa\infty} = B_{\mu\infty} = 10$ or 100, the extension rate oscillates violently with decreasing amplitude, possibly attributed to the interplay between the surface viscous

Effects	Cases	Papers
Surface viscosities play a crucial role in surfactant accumulation in secondary droplets.	$Pe = \infty$	Ponce-Torres <i>et al.</i> (2017)
Surface viscosities have a stabilizing influence on jet instability. The most unstable wavenumber depends non-monotonically on surface viscosities.	1-D and 2-D linear analysis	Martínez-Calvo & Sevilla (2018)
Surface viscous stresses enter the dominant force balance and alter the thinning rate of a thread prior to breakup.	Stokes flow, $Pe = 0$ or ∞ , $\kappa_s = \mu_s$	Wee <i>et al.</i> (2020)
Surface rheological effects do not change the power-law scalings but reduce the thinning rate in the final asymptotic regime. As the jet nears pinch-off, a balance between inertial, capillary, bulk viscous and surface viscous forces is built.	$Pe \gg 1$ or $Pe = \infty$, $\kappa_s = \mu_s$	Wee <i>et al.</i> (2021)
The critical surface Péclet number Pe_c on the boundary between diffusion-dominated region and convection-dominated region depends linearly on the Boussinesq number. When $Pe < Pe_c$, the thread thins exponentially in time; when $Pe > Pe_c$, its behaviour is self-similar and exhibits a power-law dependence on time until pinch-off.	1-D nonlinear analysis, $\kappa_s = \mu_s$	Wee <i>et al.</i> (2022)

Table 3. The effects of surface viscosities on inviscid and viscous threads.

stresses, the capillary force and the viscoelastic stresses as the thread enters the final stage. At the final stage, the filament thinning deviates from the $1/3De$ exponential law. Meanwhile, the temporal evolution of the first normal stress difference $\tau_{zz} - \tau_{rr}$ does not follow exactly the $1/3De$ exponential law, as shown in figure 11(b). The Trouton ratio η_E/η_0 behaves weirdly as well, see figure 11(d). In general, at large Boussinesq numbers, the surface viscous stresses enter the dominant force balance and affect the thinning of the filament significantly.

An interesting phenomenon is observed at moderate Boussinesq numbers. As shown in figure 11(a), for $B_{\kappa\infty} = B_{\mu\infty} = 1$, the thread radius at the midpoint, $S_{\lambda/2}$, begins to increase at some instant, indicating that a secondary droplet is formed. This is a delicate situation, for the secondary droplet disappears when the Boussinesq numbers increase a little. There seems to be a narrow window of $B_{\kappa\infty}$ and $B_{\mu\infty}$ near $O(1)$ for the appearance of secondary droplet. The surface viscosities prompt the formation of secondary droplet when they are small but suppress it when they are large.

The role of the surface viscous stresses at the final stage of thread thinning can be better understood by defining the filament Ohnesorge number $Oh_{1f}^S = \mu_s(\rho\sigma R_f^3)^{-1/2}$, where the surface shear viscosity μ_s , the surface tension σ and the filament radius R_f are all evaluated at the midpoint $z = \lambda/2$. The filament Ohnesorge number Oh_{1f}^S represents the ratio of the surface viscous stresses to the capillary force in the filament. The evolution of Oh_{1f}^S in time is shown in figures 12(a) and 12(b) for $B_{\kappa\infty} = B_{\mu\infty} = 0.1$ and $B_{\kappa\infty} = B_{\mu\infty} = 10$, respectively, where the thread radius $S_{\lambda/2}$ and the surfactant concentration $\Gamma_{\lambda/2}$ are plotted as well. As illustrated in the figure, before the final stage, Oh_{1f}^S increases slowly and $S_{\lambda/2}$ and $\Gamma_{\lambda/2}$ decrease rapidly with time increasing; in contrast, at the final stage, Oh_{1f}^S increases rapidly and $S_{\lambda/2}$ and $\Gamma_{\lambda/2}$ decrease slowly with time increasing. For the large surface Péclet number case ($Pe = 10^5$) considered in figure 12, the increase in Oh_{1f}^S at the

Dynamics of surfactant-covered viscoelastic threads

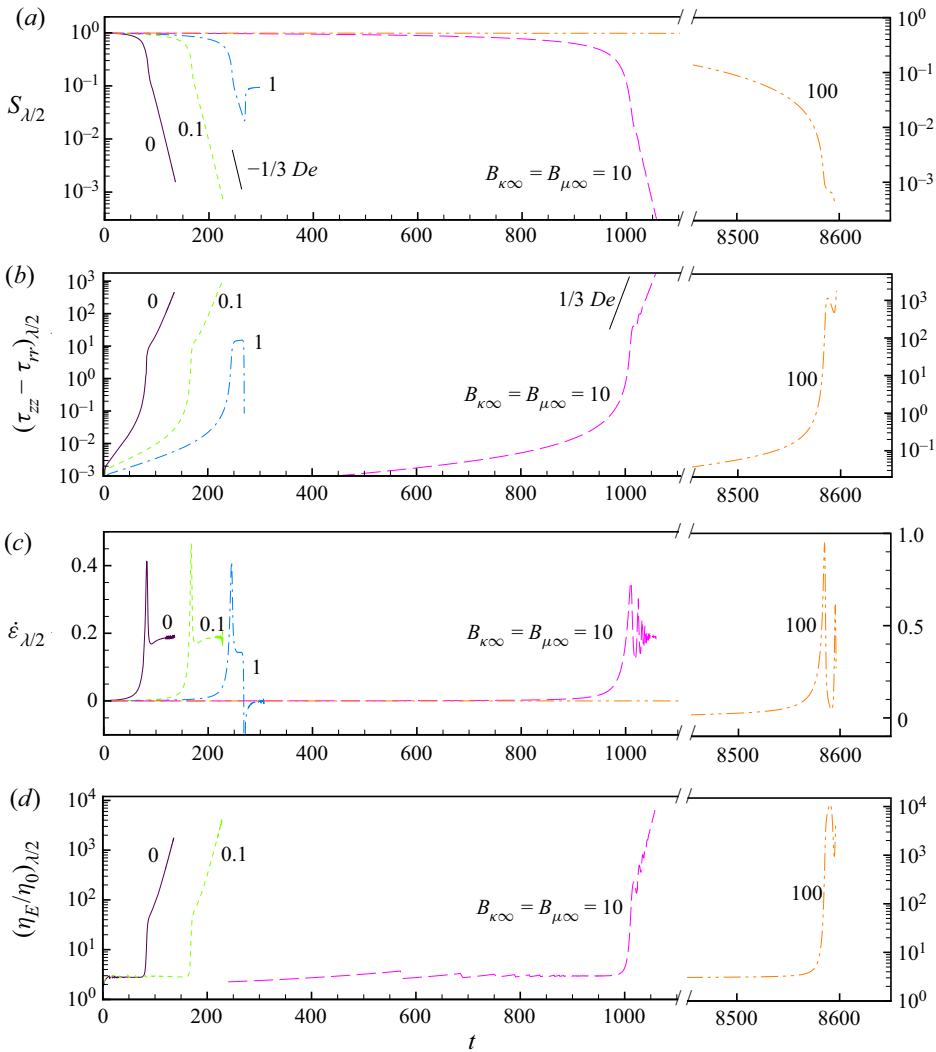


Figure 11. Effect of the Boussinesq numbers $B_{\kappa\infty}$ and $B_{\mu\infty}$ on the thinning behaviour of the Oldroyd-B viscoelastic thread, (a) the thread radius S , (b) the first normal stress difference $\tau_{zz} - \tau_{rr}$, (c) the extension rate $\dot{\epsilon}$ and (d) the Trouton ratio η_E/η_0 at the midpoint $z = \lambda/2$. The ordinate axis on the right is only for $B_{\kappa\infty} = B_{\mu\infty} = 100$ at extremely large times. Here, $k = 0.8$.

final stage, similar to the decrease in $S_{\lambda/2}$ or $\Gamma_{\lambda/2}$, seems to follow an almost exponential law in time, especially for small Boussinesq numbers. For $B_{\kappa\infty} = B_{\mu\infty} = 0.1$, Oh_{1f}^S can reach $O(1)$. For $B_{\kappa\infty} = B_{\mu\infty} = 10$, Oh_{1f}^S , which is already larger than unity at the initial time, can be $O(10^2)$ at the final time. The surface viscous stresses can still be large in the filament and compete with the capillary force and the viscoelastic stresses, even though surfactant molecules are almost swept away from the filament for large surface Péclet numbers.

The effect of the surface viscosities on the morphology of the Oldroyd-B viscoelastic thread is further examined in figure 13, where the thread profiles are plotted for different values of the axial wavenumber k . The two distinct roles of the surface viscosities can

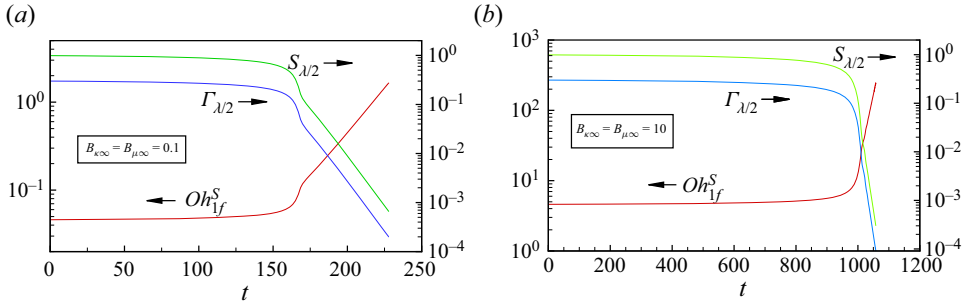


Figure 12. Temporal evolution of the filament Ohnesorge number Oh_{1f}^S , the thread radius S and the surfactant concentration Γ at the midpoint $\lambda/2$. In (a), $B_{\kappa\infty} = B_{\mu\infty} = 0.1$; in (b), $B_{\kappa\infty} = B_{\mu\infty} = 10$. Here, $k = 0.8$.

be more clearly seen in the figure. For instance, for $k = 0.7$, there exists a secondary droplet at the midpoint when the surface viscosities are absent ($B_{\kappa\infty} = B_{\mu\infty} = 0$). With the Boussinesq numbers $B_{\kappa\infty}$ and $B_{\mu\infty}$ increasing from zero, the secondary droplet is continuously shrunk. When the surface viscosities are sufficiently large, the secondary droplet completely disappears, see the thread profile for $B_{\kappa\infty} = B_{\mu\infty} = 100$, reflecting the suppression effect of the surface viscosities on secondary droplets. The same phenomenon occurs at smaller axial wavenumbers, see the thread profiles for $k = 0.3$ to 0.6 . This trend is easily understood, considering that large surface viscosities create large surface viscous stresses that tend to hinder the formation of secondary droplets. For larger axial wavenumbers $k = 0.8$ and 0.9 , the thread evolves into a beads-on-a-string structure with no secondary droplet, in the absence of surface viscosities. However, at $B_{\kappa\infty} = B_{\mu\infty} = 1$, the surface viscosities cause the appearance of a secondary droplet at the midpoint. Then, the surface viscosities try to shrink the secondary droplet and eventually lead to its disappearance, see the thread profiles for $B_{\kappa\infty} = B_{\mu\infty} = 100$. The formation of secondary droplet at large axial wavenumbers and moderate surface viscosities seems odd. It possibly results from the interplay between the inertial, capillary and surface viscous forces.

It is also found that surface viscosities can deform primary droplets. As shown in figure 13, the primary droplets are continuously stretched in the axial direction as the shear and dilatational Boussinesq numbers increase. At a value of $B_{\kappa\infty}$ and $B_{\mu\infty}$ as large as 100, the shape of the primary droplets becomes singular. The corner regions connecting the filament to the primary droplets get stretched. The shape resembles a cone in the 3-D space. From a physical point of view, the capillary force fails to overcome the surface viscous stresses and cannot help the primary droplets maintain their spheroidal shape at high surface viscosities.

In the 1-D momentum equation (3.2), the terms numbered ②, ④ and ⑤ represent the surface viscous stresses. If the shear and dilatational viscosities are not equal, terms ② and ④ are non-zero. These two terms make the simulation more difficult. To simplify the calculation, one strategy is to apply the slender body approximation to the full curvature in ② and ④, i.e.

$$\mathcal{C} \simeq \frac{1}{S}. \tag{4.16}$$

The accuracy of this simplification is checked in figure 14 by comparing the slender body approximation with the full-curvature case. It is shown in figure 14(a) that the simplification does not lead to any significant difference in the temporal evolution of the Oldroyd-B viscoelastic thread. In figures 14(b) and 14(c), the slender body approximation

Dynamics of surfactant-covered viscoelastic threads

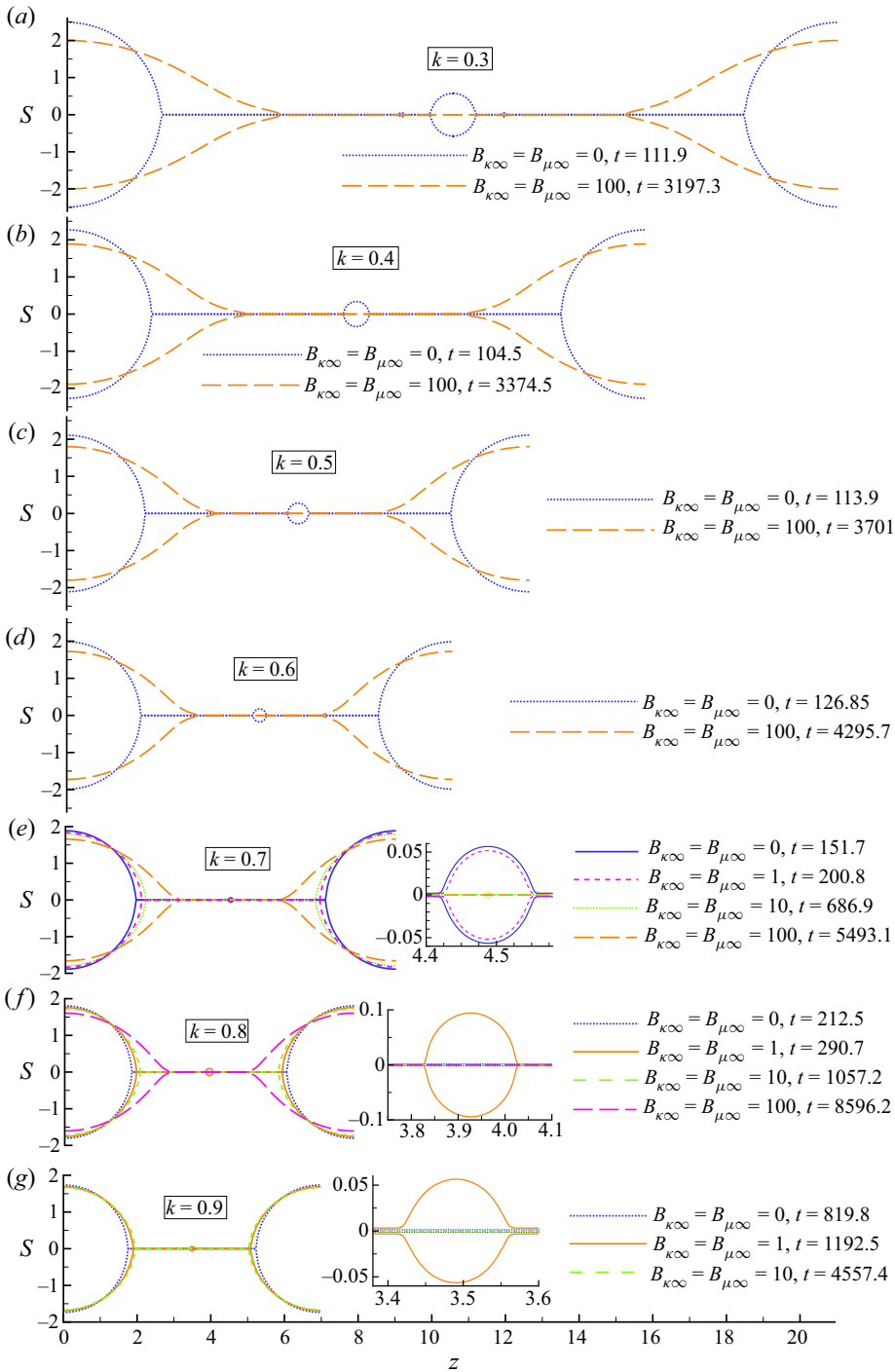


Figure 13. Thread profiles for different values of the Boussinesq numbers $B_{\kappa\infty}$ and $B_{\mu\infty}$ and different values of the axial wavenumber k . The insets illustrate the zoomed-in secondary droplet located at the midpoint $z = \lambda/2$.

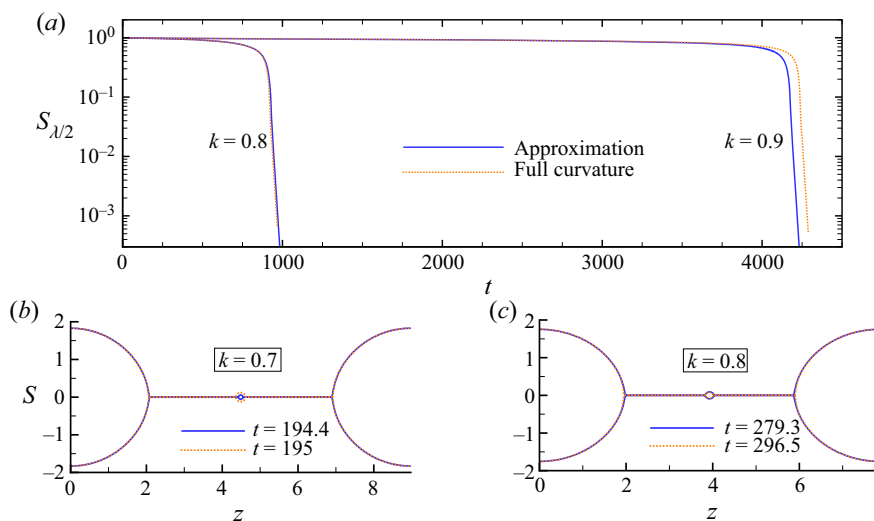


Figure 14. Comparison of the slender body approximation (solid lines) and the full-curvature (dotted lines) case. (a) Temporal evolution of the thread radius at the midpoint, $S_{\lambda/2}$, for $k = 0.8$ and 0.9 , where $B_{\kappa\infty} = 1$ and $B_{\mu\infty} = 10$; (b) and (c) thread profiles for $k = 0.7$ and $k = 0.8$, respectively, where $B_{\kappa\infty} = 0.1$ and $B_{\mu\infty} = 1$.

seems to predict smaller secondary droplets and less spherical primary droplets. Note that $B_{\kappa\infty}$ is taken to be smaller than $B_{\mu\infty}$. If $B_{\kappa\infty}$ is larger than $B_{\mu\infty}$, the trends in figures 14(b) and 14(c) are presumably opposite, since the signs of $B_{\kappa\infty}$ and $B_{\mu\infty}$ in terms ② and ④ of (3.2) are opposite.

4.3. Nonlinear behaviour of a surfactant-covered FENE-P viscoelastic thread

Different from Oldroyd-B viscoelastic threads, viscoelastic threads of FENE-P type break up in finite time, owing to finite extensibility of polymer chains. The nonlinear behaviour of a FENE-P viscoelastic thread free of surfactant is represented in figure 15. As shown in figure 15(a), the $1/3De$ exponential thinning law is valid no more for the FENE-P model. At the nonlinear stages, the elastic force in the filament fails to balance the capillary force, and the dynamics of the thread is dominated by inertia, capillarity and viscoelasticity. In such a case, the minimum radius of the thread decreases linearly in time until pinch-off. For smaller values of the finite extensibility L , the minimum thread radius S_{min} decreases faster and pinch-off occurs earlier. Meanwhile, the location of S_{min} , denoted by z_{min} , moves from the midpoint $z_{\lambda/2}$ to the corner region connecting the filament to the primary droplet, although the thickness of the filament appears to be uniform (Fontelos & Li 2004). The pinch-off time, denoted by t_p , is diagrammed in figure 15(b). It can be seen that t_p decreases as L decreases. On the other hand, t_p depends greatly on the axial wavenumber, or rather, on the growth rate predicted by linear theory. The thread profiles are plotted in figures 15(c) and 15(d) for a relatively large axial wavenumber $k = 0.8$ and a relatively small axial wavenumber $k = 0.3$, respectively. It is found that finite extensibility may alter the beads-on-a-string morphology to a certain extent. In the case of $k = 0.8$, a tiny secondary droplet arises at the midpoint when L is sufficiently small, say $L = 2$. In the case of $k = 0.3$, small extensibility may lead to large deformation of secondary droplet, see the thread profile for $L = 5$. In the following, we examine briefly the effect of surfactants on the nonlinear behaviour of FENE-P viscoelastic liquid threads.

Dynamics of surfactant-covered viscoelastic threads

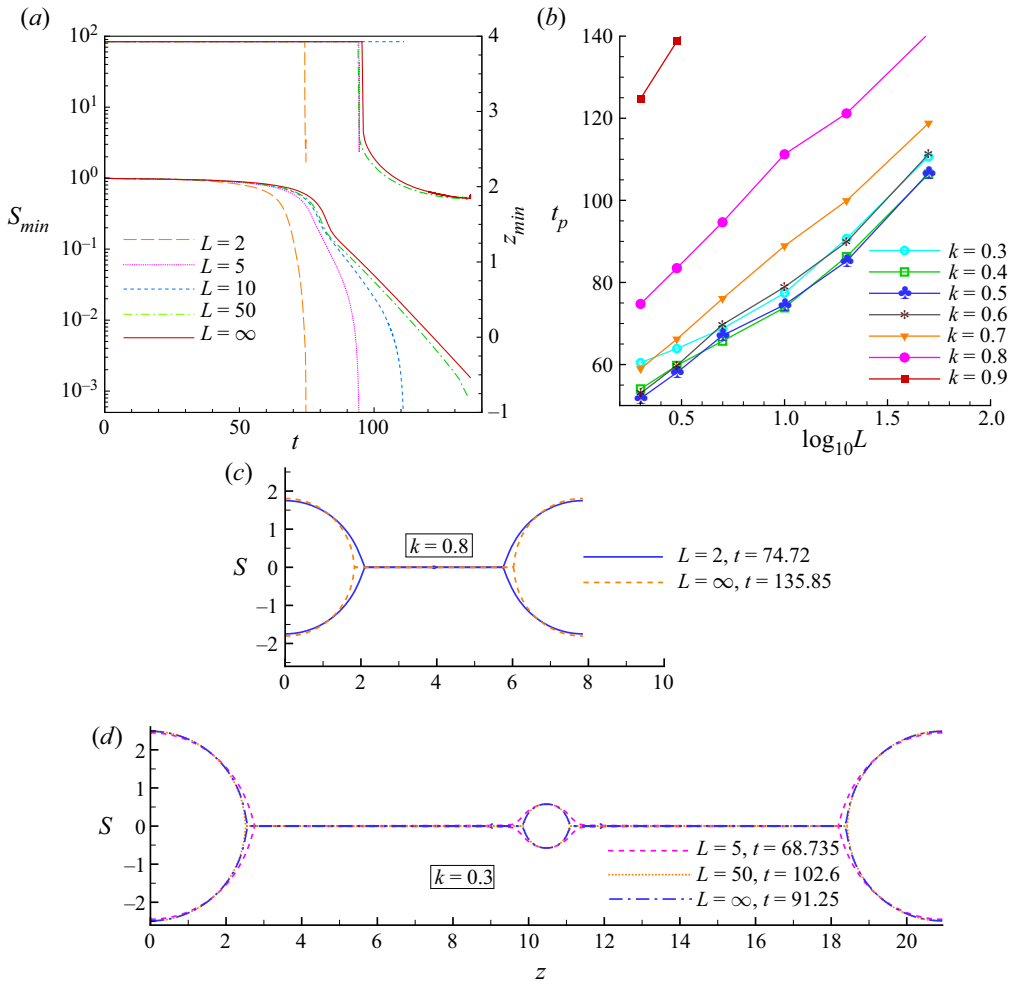


Figure 15. Effect of the finite extensibility parameter L on the nonlinear behaviour of a FENE-P viscoelastic thread free of surfactant. (a) The minimum thread radius S_{min} (the lower lines) and its location z_{min} (the upper lines) for different values of L , where $k = 0.8$. (b) The pinch-off time t_p vs L for different values of k . Thread profiles for (c) $k = 0.8$ and (d) $k = 0.3$ for different values of L .

Figure 16 illustrates the effect of the initial surfactant concentration Γ_0 on the thinning of the FENE-P viscoelastic thread. It can be seen from figure 16(a) that the surfactant retards the pinch-off of the thread. This is mainly because the decrease in the minimum thread radius S_{min} at the early stages is decelerated with increasing Γ_0 , which is basically a linear effect. At the final stage, the influence of the surfactant is limited, for most of the surfactant molecules are swept away from the filament for the large surface Péclet number case considered, as discussed in the Oldroyd-B model. In figure 16(b), close to the pinch-off time t_p , S_{min} goes to zero almost in the same way as Γ_0 varies, only that S_{min} decreases a little faster at larger values of Γ_0 .

The effect of surfactant surface diffusion on the nonlinear behaviour of the FENE-P viscoelastic thread is explored by considering the moderate surface Péclet number case $Pe = 1$. The result is illustrated in figure 17. As shown in figure 17(a), similar to the large Pe case ($Pe = 10^5$), in the moderate Pe case the pinch-off of the FENE-P viscoelastic

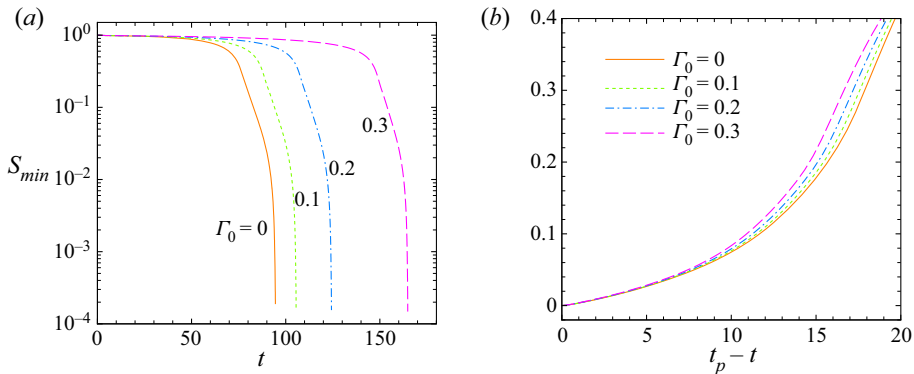


Figure 16. Effect of the initial surfactant concentration Γ_0 on the thinning of the FENE-P viscoelastic thread. (a) Temporal evolution of the minimum thread radius S_{min} and (b) S_{min} vs the time to the pinching $t_p - t$ for different values of Γ_0 . Here, $k = 0.8$.

thread is retarded by increasing the initial surfactant concentration Γ_0 , owing to the suppression effect of the surfactant on the temporal growth rate of the initial disturbance. At the nonlinear stages, the minimum thread radius S_{min} approaches zero at different speeds for different values of Γ_0 , as illustrated in figure 17(b). Unfortunately, no common trend can be found, suggesting that the surfactant affects the pinch-off of the viscoelastic thread in a complicated way.

The variation of the thread radius S , the surfactant concentration Γ , the surface tension σ , the axial velocity u and the first normal stress difference $\tau_{zz} - \tau_{rr}$ along the thread is illustrated in figure 17(c) for the axial wavenumber $k = 0.8$ and the initial surfactant concentration $\Gamma_0 = 0$ and 0.3. The spatial variation of u and $\tau_{zz} - \tau_{rr}$ suggests that a tiny secondary droplet arises at the midpoint $z = \lambda/2$ in the absence of the surfactant ($\Gamma_0 = 0$), although it is almost invisible from the thread profile. In the presence of the surfactant, i.e. $\Gamma_0 = 0.3$, the volume of the secondary droplet is visibly increased. Due to surface diffusion, surfactant molecules cover the entire thread densely. Particularly in the neighbourhood of the secondary droplet, the surfactant concentration Γ is close to unity and the surface tension σ is very small. Correspondingly, the viscoelastic force in the neighbourhood of the secondary droplet is small and the secondary droplet deforms greatly from spherical.

The effect of the initial surfactant concentration Γ_0 on the beads-on-a-string morphology in the moderate Pe case can be seen from figures 17(d) and 17(e) for the relatively large axial wavenumber $k = 0.8$ and the relatively small axial wavenumber $k = 0.4$, respectively. For both wavenumbers, the secondary droplet at the midpoint gains weight and exhibits a more singular shape as Γ_0 increases. Meanwhile, the thickness of the filament becomes more non-uniform. Pinch-off always occurs at the corner region where the filament joins the primary droplet. For the relatively small axial wavenumber $k = 0.4$, higher-order generations of secondary droplets can be formed at sufficiently large values of Γ_0 (see the thread profile for $\Gamma_0 = 0.5$).

The effect of the Marangoni stress on the pinch-off of the FENE-P viscoelastic thread is examined in figure 18, by comparing the case in which the Marangoni stress is taken into account with the case in which the Marangoni stress is turned off. As seen in figure 18(a), for the relatively large axial wavenumber $k = 0.8$, the pinch-off of the viscoelastic thread occurs much earlier when the Marangoni stress is turned off. Note that the two lines intersect with each other near $S_{min} = 0.53$ and $t_p - t = 23$. Before

Dynamics of surfactant-covered viscoelastic threads

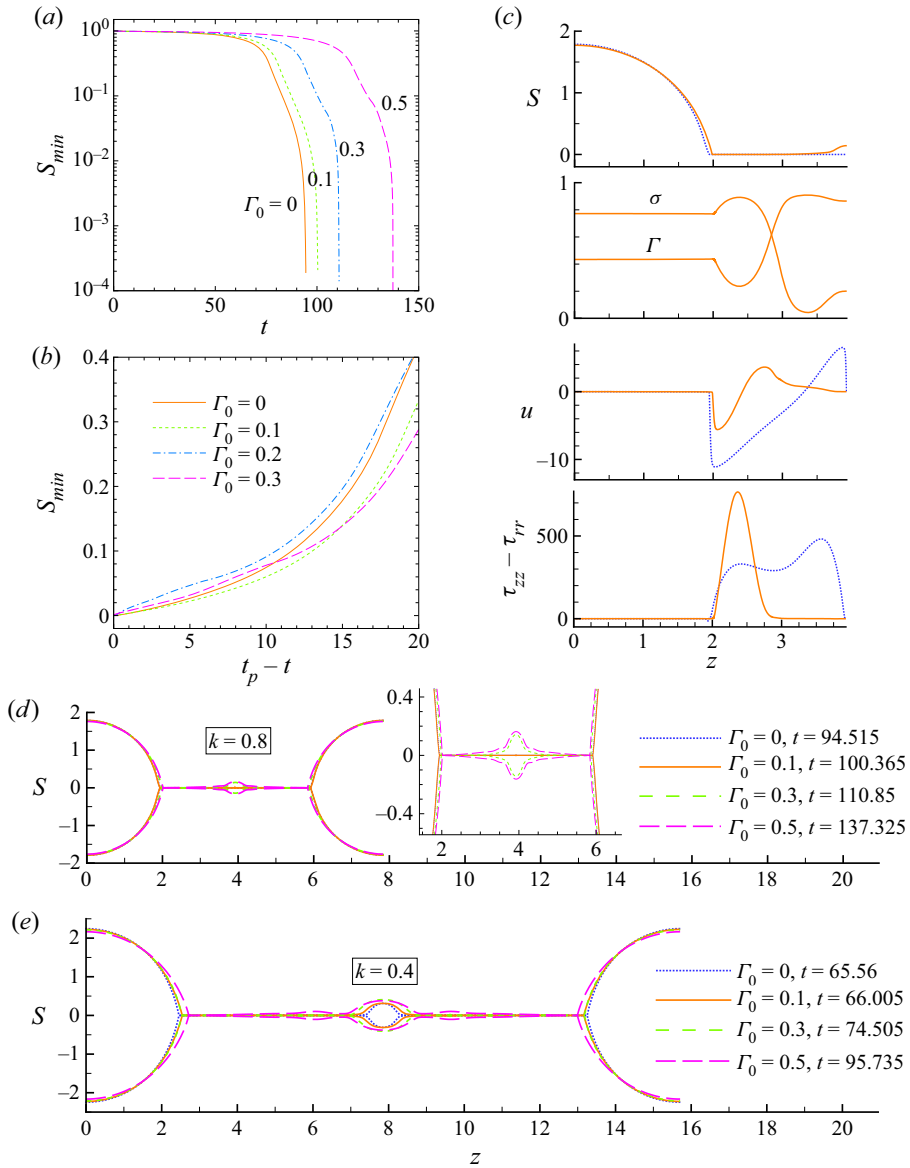


Figure 17. The case of moderate surface Péclet number $Pe = 1$. (a) Temporal evolution of the minimum thread radius S_{min} and (b) S_{min} vs the time to the pinching $t_p - t$ for distinct values of the initial surfactant concentration Γ_0 . (c) Spatial variation of the thread radius S , the surfactant concentration Γ , the surface tension σ , the axial velocity u and the first normal stress difference $\tau_{zz} - \tau_{rr}$ along the thread. In (a–c), $k = 0.8$. In (c), the solid lines are for $\Gamma_0 = 0.3$ (the time instant $t = 110.795$) and the dotted lines are for $\Gamma_0 = 0$ ($t = 94.48$). (d) Thread profiles for $k = 0.8$ and distinct values of Γ_0 , where the inset is the zoomed-in filament and secondary droplet regions. (e) Thread profiles for $k = 0.4$ and distinct values of Γ_0 .

intersecting, the minimum thread radius S_{min} decreases much more rapidly in the absence of the Marangoni stress. In contrast, from the intersection point, it takes S_{min} the same time in two cases to decrease to zero. In general, the Marangoni stress greatly delays the pinch-off of the FENE-P viscoelastic thread. The thread profiles prior to pinch-off are plotted in figures 18(b) and 18(c) for $k = 0.8$ and 0.3 , respectively. For both axial

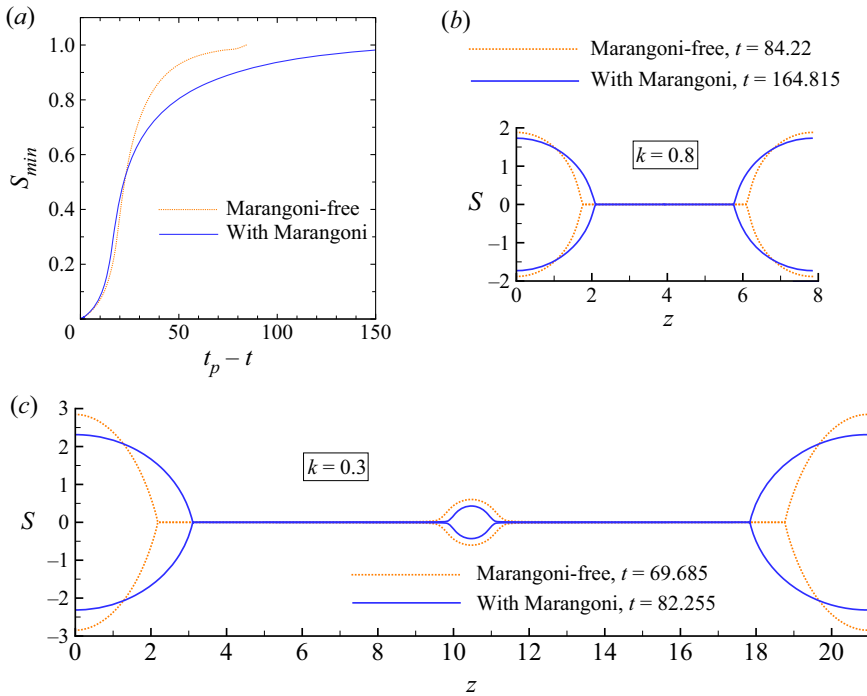


Figure 18. Effect of the Marangoni stress on the nonlinear behaviour of the FENE-P viscoelastic thread. (a) The minimum thread radius S_{min} vs the time to the pinching $t_p - t$ for $k = 0.8$. Thread profiles for (b) $k = 0.8$ and (c) $k = 0.3$.

wavenumbers, the primary droplets have been axially stretched by the Marangoni stress before the pinch-off takes place. The secondary droplets remain singular in shape when the Marangoni stress is absent. It indicates that the Marangoni stress has little to do with the non-spherical shape of secondary droplets. The deformation of secondary droplets possibly results from small local surface tension. On the other hand, the Marangoni stress affects secondary droplets by reducing their size.

Figure 19 shows the effect of the Marangoni number E on the pinch-off of the FENE-P viscoelastic thread. At the early stages, the thinning of the thread can be greatly slowed down by increasing the value of E , owing to the suppression effect of the Marangoni number on the linear instability of the thread. At the late stages, from approximately $S_{min} = 0.45$ and $t_p - t = 21$, the effect of the Marangoni number becomes quite limited. Recall that in the large surface Péclet number case of the Oldroyd-B viscoelastic thread, surfactant molecules are continuously convected to the primary droplet and not many remain at the filament surface. The situation is similar for the FENE-P viscoelastic thread.

In addition to the Marangoni number E , the Boussinesq numbers $B_{\kappa\infty}$ and $B_{\mu\infty}$ may greatly delay the pinch-off of the FENE-P viscoelastic thread, as illustrated in figure 20(a). At relatively small values of $B_{\kappa\infty}$ and $B_{\mu\infty}$ such as 0.1 and 1, the surface viscosities slow down the growth of the initial disturbance at the early stages. At relatively large values of $B_{\kappa\infty}$ and $B_{\mu\infty}$ 10 and 100, the surface viscosities tend to inhibit the pinch-off of the viscoelastic thread. The thread profiles for the axial wavenumber $k = 0.3$ and several values of $B_{\kappa\infty}$ and $B_{\mu\infty}$ are plotted in figure 20(b). Like in Oldroyd-B threads, the surface viscous stresses may lead to the axial stretch of primary droplets. When $B_{\kappa\infty}$ and $B_{\mu\infty}$ are large, e.g. $B_{\kappa\infty} = B_{\mu\infty} = 10$, the corner connecting the filament to the primary droplet is

Dynamics of surfactant-covered viscoelastic threads

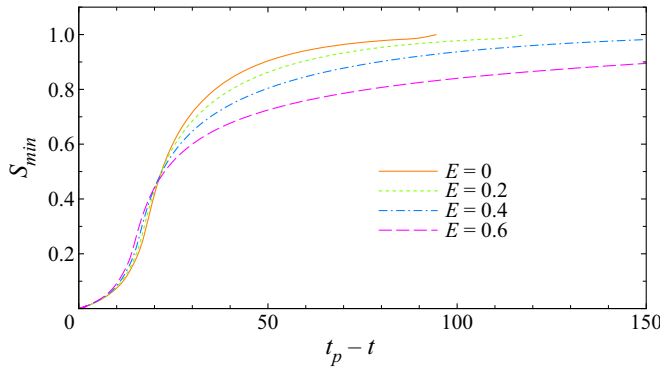


Figure 19. Effect of the Marangoni number E on the pinch-off of the FENE-P viscoelastic thread. The minimum thread radius S_{min} vs the time to the pinching $t_p - t$. Here, $k = 0.8$.

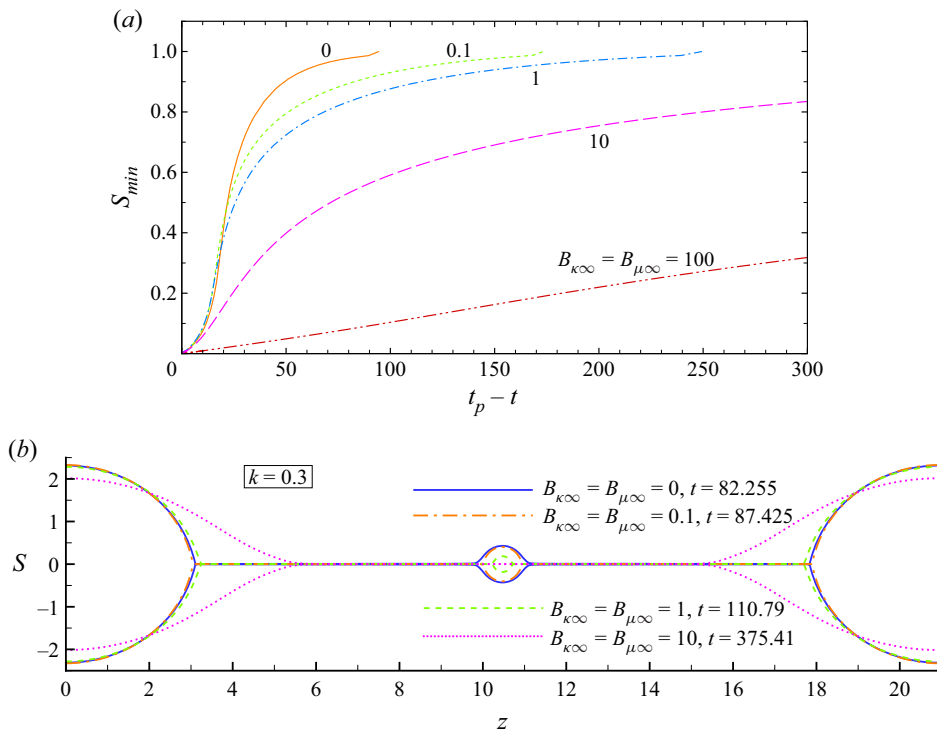


Figure 20. Effect of the Boussinesq numbers $B_{\kappa\infty}$ and $B_{\mu\infty}$ on the pinch-off of the FENE-P viscoelastic thread. (a) The minimum thread radius S_{min} vs the time to the pinching $t_p - t$ for $k = 0.8$. (b) Thread profiles for different values of $B_{\kappa\infty}$ and $B_{\mu\infty}$, $k = 0.3$.

axially stretched and the primary droplet is greatly deformed. On the other hand, for this small axial wavenumber, the secondary droplet located at the midpoint loses weight under the action of the surface viscous stresses. At sufficiently large values of $B_{\kappa\infty}$ and $B_{\mu\infty}$, the secondary droplet disappears.

5. Conclusion

Based on the slender body theory, we develop a 1-D model to numerically study the effect of an insoluble surfactant monolayer on the nonlinear dynamics of a non-Newtonian viscoelastic thread of Oldroyd-B or FENE-P type. In particular, we take into account the surface rheological properties of the surfactant. There are five dimensionless numbers related to the surfactant, i.e. the initial surfactant concentration, the Marangoni number, the surface Péclet number, the dilatational Boussinesq number and the shear Boussinesq number. The effect of these dimensionless numbers on the dynamics of the viscoelastic thread initially perturbed by a small harmonic disturbance is examined one by one.

The 1-D linear instability result shows that the temporal growth rate of the disturbance can be decreased by increasing the initial surfactant concentration, the Marangoni number, the surface Péclet number, the dilatational Boussinesq number or the shear Boussinesq number. That is, the presence of the surfactant suppresses the linear instability of the viscoelastic thread in all ways. The suppression effect of the surfactant is profound. It can greatly postpone the late nonlinear stages of thread thinning.

The surface Péclet number plays an important role in the nonlinear evolution of the viscoelastic thread. At large values of the surface Péclet number, the surfactant has a negligible influence on the exponential thinning of the Oldroyd-B viscoelastic thread, owing to the evacuation of surfactant molecules from the filament under the dominance of surface convection. On the other hand, the surfactant may affect the beads-on-a-string structure in two ways: it decreases the size of the secondary droplet or even remove it completely when the initial surfactant concentration or the Marangoni number is large enough; it stretches the primary droplet in the axial direction and leads to its deformation from a spherical to a prolate shape. In these phenomena, the Marangoni stress plays a role. At moderate values of the surface Péclet number, surfactant molecules are distributed over the filament due to surface diffusion, leading to the formation of secondary droplet in the filament.

At large values of the shear and dilatational Boussinesq numbers, the thinning of the viscoelastic thread can be greatly delayed by the surface viscous stresses. At the final stage, besides the capillary and elastic forces, the surface viscous stresses enter the dominant force balance in the filament. The filament follows the $1/3De$ exponential law no more. On the other hand, the surface viscous stresses can lead to the decrease in the secondary droplet size. When the Boussinesq numbers are sufficiently large, the secondary droplet disappears. Larger surface viscous stresses also lead to larger deformation of primary droplets.

The pinch-off of the FENE-P viscoelastic thread can be greatly delayed by the presence of the surfactant. Prior to pinch-off, the decrease in the minimum thread radius is little influenced by the surfactant, if the surface Péclet number is large. However, when surface diffusion is important, the surfactant affects the pinch-off of the thread in a complicated way. The effect of the surfactant on the beads-on-a-string morphology of the FENE-P viscoelastic thread is similar to that on the Oldroyd-B viscoelastic thread.

According to the 1-D simulation, for surfactant-covered viscoelastic threads, the corner region connecting the primary droplet to the filament may possess self-similarity. An exploration of self-similar solutions may be performed in the future, taking into account the Marangoni stress and/or the surface rheological properties. Another open problem is the deformation of primary droplets driven by the surface viscous stresses. The singular shape of primary droplets is rare and deserves more investigation. In addition, it is of interest to develop an improved 1-D model with all necessary high-order terms

included. The numerical simulation of the 2-D axisymmetric nonlinear dynamics of surfactant-covered viscoelastic threads needs to be carried out to verify the 1-D results.

Acknowledgements. We thank all the reviewers for their constructive comments and suggestions.

Funding. F.L. was supported by the National Natural Science Foundation of China (nos 12272373 and 11621202). D.H. was supported by the National Natural Science Foundation of China (no. 12172317), Guangdong Basic and Applied Basic Research Foundation (grant no. 2022A1515011784), and Shenzhen Science and Technology Program (no. JCYJ20210324125601005).

Declaration of interests. The authors report no conflict of interest.

Author ORCIDs.

 Fang Li <https://orcid.org/0000-0001-9825-0101>;

 Dongdong He <https://orcid.org/0000-0002-5786-581X>.

Appendix A. Derivation of the 1-D equations

The characteristic length in the radial direction, l_r , is assumed to be much smaller than the characteristic length in the axial direction, l_z , i.e.

$$l_r = \varepsilon l_z, \tag{A1}$$

where ε is a small parameter. The balance of the capillary, inertial and viscoelastic forces gives

$$\rho \frac{l_z}{l_t^2} = \eta_0 \frac{l_r/l_t}{l_z^2} = \frac{\sigma_0}{l_r} \frac{1}{l_z}. \tag{A2}$$

Use the scales

$$\left. \begin{aligned} r &= l_r \tilde{r}, \quad z = l_z \tilde{z}, \quad t = l_t \tilde{t}, \quad S = l_r \tilde{S}, \quad v = \frac{l_r}{l_t} \tilde{v}, \quad u = \frac{l_z}{l_t} \tilde{u}, \quad \sigma = \sigma_0 \tilde{\sigma}, \quad p = \frac{\rho l_z^2}{l_t^2} \tilde{p}, \\ \tau_{rr} &= \frac{\rho l_z^2}{l_t^2} \tilde{\tau}_{rr}, \quad \tau_{\theta\theta} = \frac{\rho l_z^2}{l_t^2} \tilde{\tau}_{\theta\theta}, \quad \tau_{zz} = \frac{\rho l_z^2}{l_t^2} \tilde{\tau}_{zz}, \quad \tau_{rz} = \frac{\rho l_z^3}{l_r l_t^2} \tilde{\tau}_{rz}, \quad \Gamma = \Gamma_\infty \tilde{\Gamma}, \end{aligned} \right\} \tag{A3}$$

where the tilde denotes the corresponding dimensionless quantities. Hereafter the tilde is dropped for brevity.

The continuity, momentum and constitutive equations (2.1)–(2.10) are non-dimensionalized as

$$\frac{1}{r} \frac{\partial(rv)}{\partial r} + \frac{\partial u}{\partial z} = 0, \tag{A4}$$

$$\begin{aligned} \frac{\partial v}{\partial t} + v \frac{\partial v}{\partial r} + u \frac{\partial v}{\partial z} &= -\frac{1}{\varepsilon^2} \frac{\partial p}{\partial r} + \frac{\beta}{\varepsilon^2} \left(\frac{\partial^2 v}{\partial r^2} + \frac{1}{r} \frac{\partial v}{\partial r} - \frac{v}{r^2} \right) + \beta \frac{\partial^2 v}{\partial z^2} \\ &+ \frac{1}{\varepsilon^2} \left(\frac{\partial \tau_{rr}}{\partial r} + \frac{\partial \tau_{rz}}{\partial z} + \frac{\tau_{rr} - \tau_{\theta\theta}}{r} \right), \end{aligned} \tag{A5}$$

$$\frac{\partial u}{\partial t} + v \frac{\partial u}{\partial r} + u \frac{\partial u}{\partial z} = -\frac{\partial p}{\partial z} + \frac{\beta}{\varepsilon^2} \left(\frac{\partial^2 u}{\partial r^2} + \frac{1}{r} \frac{\partial u}{\partial r} \right) + \beta \frac{\partial^2 u}{\partial z^2} + \frac{1}{\varepsilon^2} \frac{\partial \tau_{rz}}{\partial r} + \frac{1}{\varepsilon^2} \frac{\tau_{rz}}{r} + \frac{\partial \tau_{zz}}{\partial z}, \tag{A6}$$

$$\tau_{zz} = \frac{1 - \beta}{De} \left(\frac{A_{zz}}{1 - \frac{tr(\mathbf{A})}{L^2}} - 1 \right), \tag{A7}$$

$$\tau_{rr} = \frac{1 - \beta}{De} \left(\frac{A_{rr}}{1 - \frac{tr(\mathbf{A})}{L^2}} - 1 \right), \tag{A8}$$

$$\tau_{\theta\theta} = \frac{1 - \beta}{De} \left(\frac{A_{\theta\theta}}{1 - \frac{tr(\mathbf{A})}{L^2}} - 1 \right), \tag{A9}$$

$$\tau_{rz} = \frac{1 - \beta}{De} \frac{A_{rz}}{1 - \frac{tr(\mathbf{A})}{L^2}}, \tag{A10}$$

$$De \left(\frac{\partial A_{zz}}{\partial t} + v \frac{\partial A_{zz}}{\partial r} + u \frac{\partial A_{zz}}{\partial z} - \frac{2}{\varepsilon^2} A_{rz} \frac{\partial u}{\partial r} - 2A_{zz} \frac{\partial u}{\partial z} \right) = 1 - \frac{A_{zz}}{1 - \frac{tr(\mathbf{A})}{L^2}}, \tag{A11}$$

$$De \left(\frac{\partial A_{rr}}{\partial t} + v \frac{\partial A_{rr}}{\partial r} + u \frac{\partial A_{rr}}{\partial z} - 2A_{rr} \frac{\partial v}{\partial r} - 2A_{rz} \frac{\partial v}{\partial z} \right) = 1 - \frac{A_{rr}}{1 - \frac{tr(\mathbf{A})}{L^2}}, \tag{A12}$$

$$De \left(\frac{\partial A_{\theta\theta}}{\partial t} + v \frac{\partial A_{\theta\theta}}{\partial r} + u \frac{\partial A_{\theta\theta}}{\partial z} - 2A_{\theta\theta} \frac{v}{r} \right) = 1 - \frac{A_{\theta\theta}}{1 - \frac{tr(\mathbf{A})}{L^2}}, \tag{A13}$$

$$De \left(\frac{\partial A_{rz}}{\partial t} + v \frac{\partial A_{rz}}{\partial r} + u \frac{\partial A_{rz}}{\partial z} - A_{rr} \frac{\partial u}{\partial r} - \varepsilon^2 A_{zz} \frac{\partial v}{\partial z} \right) = - \frac{A_{rz}}{1 - \frac{tr(\mathbf{A})}{L^2}}, \tag{A14}$$

where $De = \lambda_c/l_t$ and $\beta = \eta_s/\eta_0 = \eta_s/(\eta_s + \eta_p)$.

The non-dimensionalized advection–diffusion equation for the surfactant is

$$\begin{aligned} \frac{\partial \Gamma}{\partial t} + u \frac{\partial \Gamma}{\partial z} + \frac{\Gamma}{S\sqrt{1 + \varepsilon^2 S'^2}} \frac{\partial \left(\frac{S(u + \varepsilon^2 v S')}{\sqrt{1 + \varepsilon^2 S'^2}} \right)}{\partial z} + C\Gamma \frac{v - uS'}{\sqrt{1 + \varepsilon^2 S'^2}} \\ = \frac{1}{Pe} \frac{1}{S\sqrt{1 + S'^2}} \frac{\partial \left(\frac{S\Gamma'}{\sqrt{1 + \varepsilon^2 S'^2}} \right)}{\partial z}, \end{aligned} \tag{A15}$$

where $Pe = l_z^2/D_s l_t$ and $C = 1/S\sqrt{1 + \varepsilon^2 S'^2} - \varepsilon^2 S''/(1 + \varepsilon^2 S'^2)^{3/2}$.

The non-dimensionalized kinematic boundary condition at the surface $r = S(z, t)$ has the same form with the dimensional one, i.e.

$$v = \frac{\partial S}{\partial t} + u \frac{\partial S}{\partial z}. \tag{A16}$$

The normal and tangential force balance at the surface is non-dimensionalized as

$$\begin{aligned}
 p - \frac{1}{1 + \varepsilon^2 S'^2} \left[2\beta \frac{\partial v}{\partial r} - 2\beta S' \left(\varepsilon^2 \frac{\partial v}{\partial z} + \frac{\partial u}{\partial r} \right) + 2\beta \varepsilon^2 S'^2 \frac{\partial u}{\partial z} + \varepsilon^2 S'^2 \tau_{zz} - 2S' \tau_{rz} + \tau_{rr} \right] \\
 = \mathcal{C} \left[\sigma + (B_{\kappa\infty} \kappa_s - B_{\mu\infty} \mu_s) \left(\frac{(Su_t)'}{S\sqrt{1 + \varepsilon^2 S'^2}} + \mathcal{C}u_n \right) \right] \\
 + \frac{2B_{\mu\infty} \mu_s}{1 + \varepsilon^2 S'^2} \left[\frac{S'u_t + u_n}{S^2} - \frac{\varepsilon^2 S''}{1 + \varepsilon^2 S'^2} \left(\frac{\partial(u_t)}{\partial z} - \frac{\varepsilon^2 S'' u_n}{1 + \varepsilon^2 S'^2} \right) \right], \tag{A17}
 \end{aligned}$$

and

$$\begin{aligned}
 \frac{1}{(1 + \varepsilon^2 S'^2)} \left[2\varepsilon^2 \beta S' \left(\frac{\partial v}{\partial r} - \frac{\partial u}{\partial z} \right) + \beta (1 - \varepsilon^2 S'^2) \left(\varepsilon^2 \frac{\partial v}{\partial z} + \frac{\partial u}{\partial r} \right) \right] \\
 + \frac{1}{(1 + \varepsilon^2 S'^2)} [\varepsilon^2 (\tau_{rr} - \tau_{zz}) S' + (1 - \varepsilon^2 S'^2) \tau_{rz}] \\
 = \varepsilon^2 \frac{\partial \sigma}{\partial z} + \varepsilon^2 \frac{\partial}{\partial z} \left[(B_{\kappa\infty} \kappa_s - B_{\mu\infty} \mu_s) \left(\frac{(Su_t)'}{S\sqrt{1 + \varepsilon^2 S'^2}} \right) + \mathcal{C}u_n \right] \\
 + \frac{\varepsilon^2 \sqrt{1 + \varepsilon^2 S'^2}}{S} \frac{\partial}{\partial z} \left[\frac{2B_{\mu\infty} \mu_s S}{1 + \varepsilon^2 S'^2} \left(\frac{\partial u_t}{\partial z} - \frac{\varepsilon^2 S'' u_n}{1 + \varepsilon^2 S'^2} \right) \right] \\
 - \frac{2\varepsilon^2 B_{\mu\infty} \mu_s S'}{\sqrt{1 + \varepsilon^2 S'^2}} \left[\frac{S'u_t + u_n}{S^2} - \frac{\varepsilon^2 S''}{1 + \varepsilon^2 S'^2} \left(\frac{\partial u_t}{\partial z} - \frac{\varepsilon^2 S'' u_n}{1 + \varepsilon^2 S'^2} \right) \right], \tag{A18}
 \end{aligned}$$

where $B_{\kappa\infty} = \kappa_{s\infty}/l_r \eta_0$ with $\kappa_{s\infty}$ the surface dilatational viscosity at $\Gamma = \Gamma_\infty$, $B_{\mu\infty} = \mu_{s\infty}/l_r \eta_0$ with $\mu_{s\infty}$ the surface shear viscosity at $\Gamma = \Gamma_\infty$ and $\sigma = 1 + E \ln(1 - \Gamma)$ with $E = R_g T \Gamma_\infty / \sigma_0$.

Expand the quantities into Taylor series of εr

$$u(r, z, t) = u_0(z, t) + u_2(z, t) \frac{(\varepsilon r)^2}{2} + \dots, \tag{A19}$$

$$v(r, z, t) = -\frac{r}{2} \frac{\partial u_0}{\partial z} - \frac{\varepsilon^2 r^3}{8} \frac{\partial u_2(z, t)}{\partial z} + \dots, \tag{A20}$$

$$p(r, z, t) = p_0(z, t) + p_2(z, t) (\varepsilon r)^2 + \dots, \tag{A21}$$

$$\tau_{rr}(r, z, t) = \tau_{rr0}(z, t) + \tau_{rr2}(z, t) (\varepsilon r)^2 + \dots, \tag{A22}$$

$$\tau_{zz}(r, z, t) = \tau_{zz0}(z, t) + \tau_{zz2}(z, t) (\varepsilon r)^2 + \dots, \tag{A23}$$

$$\tau_{\theta\theta}(r, z, t) = \tau_{\theta\theta0}(z, t) + \tau_{\theta\theta2}(z, t) (\varepsilon r)^2 + \dots, \tag{A24}$$

$$r\tau_{rz}(r, z, t) = \tau_{rz0}(z, t) + \tau_{rz2}(z, t) (\varepsilon r)^2 + \dots. \tag{A25}$$

$$A_{rr}(r, z, t) = A_{rr0}(z, t) + A_{rr2}(z, t) (\varepsilon r)^2 + \dots, \tag{A26}$$

$$A_{zz}(r, z, t) = A_{zz0}(z, t) + A_{zz2}(z, t) (\varepsilon r)^2 + \dots, \tag{A27}$$

$$A_{\theta\theta}(r, z, t) = A_{\theta\theta0}(z, t) + A_{\theta\theta2}(z, t) (\varepsilon r)^2 + \dots, \tag{A28}$$

$$rA_{rz}(r, z, t) = A_{rz0}(z, t) + A_{rz2}(z, t) (\varepsilon r)^2 + \dots. \tag{A29}$$

Substituting the expansions (A19)–(A29) into the kinematic condition (A16), the leading order yields

$$v_0(S, z, t) = \frac{\partial S}{\partial t} + u_0 \frac{\partial S}{\partial z} = -\frac{S}{2} \frac{\partial u_0}{\partial z}. \tag{A30}$$

Thus

$$\frac{\partial(S^2)}{\partial t} + \frac{\partial(S^2 u_0)}{\partial z} = 0. \tag{A31}$$

Substituting the expansions (A19)–(A29) into (A4)–(A14), we have $\tau_{rz0} = 0$, $\tau_{rr0} = \tau_{\theta\theta0}$, $A_{rz0} = 0$, $A_{rr0} = A_{\theta\theta0}$ and

$$\frac{\partial u_0}{\partial t} + u_0 \frac{\partial u_0}{\partial z} = -\frac{\partial p_0}{\partial z} + \beta \left(2u_2 + \frac{\partial^2 u_0}{\partial z^2} \right) + 2\tau_{rz2} + \frac{\partial \tau_{zz0}}{\partial z}, \tag{A32}$$

$$\tau_{zz0} = \frac{1 - \beta}{De} \left(\frac{A_{zz0}}{1 - \frac{tr(\mathbf{A}_0)}{L^2}} - 1 \right), \tag{A33}$$

$$\tau_{rr0} = \frac{1 - \beta}{De} \left(\frac{A_{rr0}}{1 - \frac{tr(\mathbf{A}_0)}{L^2}} - 1 \right), \tag{A34}$$

$$De \left(\frac{\partial A_{zz0}}{\partial t} + u_0 \frac{\partial A_{zz0}}{\partial z} - 2A_{zz0} \frac{\partial u_0}{\partial z} \right) = 1 - \frac{A_{zz0}}{1 - \frac{tr(\mathbf{A}_0)}{L^2}}, \tag{A35}$$

$$De \left(\frac{\partial A_{rr0}}{\partial t} + u_0 \frac{\partial A_{rr0}}{\partial z} + A_{rr0} \frac{\partial u_0}{\partial z} \right) = 1 - \frac{A_{rr0}}{1 - \frac{tr(\mathbf{A}_0)}{L^2}}, \tag{A36}$$

where $tr(\mathbf{A}_0) = A_{zz0} + 2A_{rr0}$.

The surfactant conservation equation (A15) at $O(1)$ gives

$$\frac{\partial \Gamma}{\partial t} + u_0 \frac{\partial \Gamma}{\partial z} - \frac{C\Gamma}{2S} \frac{\partial(S^2 u_0)}{\partial z} = \frac{1}{Pe} \frac{1}{S} \frac{\partial(S\Gamma')}{\partial z}. \tag{A37}$$

The normal force balance (A17) at $O(1)$ gives

$$p_0 = \tau_{rr0} - \beta \frac{\partial u_0}{\partial z} + C \left[\sigma + \frac{B_{\kappa\infty} \kappa_s - B_{\mu\infty} \mu_s}{S} \left(\frac{\partial(u_0 S)}{\partial z} - \frac{C}{2} \frac{\partial(u_0 S^2)}{\partial z} \right) \right] - \frac{B_{\mu\infty} \mu_s}{S} \frac{\partial u_0}{\partial z}. \tag{A38}$$

The derivative of (A38) with respect to z is

$$-\frac{\partial p_0}{\partial z} = -\frac{\partial \tau_{rr0}}{\partial z} + \beta \frac{\partial^2 u_0}{\partial z^2} - \frac{\partial}{\partial z} \left[C \left(\sigma + \frac{B_{\kappa\infty} \kappa_s - B_{\mu\infty} \mu_s}{S} \left(\frac{\partial(u_0 S)}{\partial z} - \frac{C}{2} \frac{\partial(u_0 S^2)}{\partial z} \right) \right) \right] + B_{\mu\infty} \frac{\partial}{\partial z} \left[\frac{\mu_s u'_0}{S} \right]. \tag{A39}$$

The tangential force balance (A18) at $O(\varepsilon^2)$ gives

$$\begin{aligned} \beta u_2 + \tau_{rz2} &= \frac{3\beta S'}{S} \frac{\partial u_0}{\partial z} + \frac{\beta}{2} \frac{\partial^2 u_0}{\partial z^2} - \frac{S'}{S} (\tau_{rr0} - \tau_{zz0}) \\ &\quad \frac{1}{S} \left\{ \frac{\partial \sigma}{\partial z} + \frac{\partial}{\partial z} \left[\frac{B_{\kappa\infty} \kappa_s - B_{\mu\infty} \mu_s}{S} \left(\frac{\partial(u_0 S)}{\partial z} - \frac{C}{2} \frac{\partial(u_0 S^2)}{\partial z} \right) \right] \right\} \\ &\quad + \frac{2B_{\mu\infty}}{S^2} \frac{\partial(\mu_s S u_0')}{\partial z} + \frac{B_{\mu\infty} \mu_s}{S^2} \frac{\partial u_0}{\partial z} S'. \end{aligned} \tag{A40}$$

Substituting (A39) and (A40) into (A32) yields

$$\begin{aligned} \frac{\partial u_0}{\partial t} + u_0 \frac{\partial u_0}{\partial z} &= \frac{3\beta}{S^2} \frac{\partial(S^2 u_0')}{\partial z} + \frac{1}{S^2} \frac{\partial[S^2(\tau_{zz0} - \tau_{rr0})]}{\partial z} \\ &\quad - \frac{\partial}{\partial z} \left\{ C \left[\sigma + \frac{B_{\kappa\infty} \kappa_s - B_{\mu\infty} \mu_s}{S} \left(\frac{\partial(u_0 S)}{\partial z} - \frac{C}{2} \frac{\partial(u_0 S^2)}{\partial z} \right) \right] \right\} \\ &\quad + \frac{2}{S} \left\{ \frac{\partial \sigma}{\partial z} + \frac{\partial}{\partial z} \left[\frac{B_{\kappa\infty} \kappa_s - B_{\mu\infty} \mu_s}{S} \left(\frac{\partial(u_0 S)}{\partial z} - \frac{C}{2} \frac{\partial(u_0 S^2)}{\partial z} \right) \right] \right\} \\ &\quad + \frac{5B_{\mu\infty}}{S^2} \frac{\partial(\mu_s S u_0')}{\partial z}. \end{aligned} \tag{A41}$$

Equations (A31), (A33)–(A37) and (A41) constitute the 1-D model. Dropping the subscript 0, we have

$$\frac{\partial S^2}{\partial t} + \frac{\partial(S^2 u)}{\partial z} = 0, \tag{A42}$$

$$\begin{aligned} \rho \left(\frac{\partial u}{\partial t} + u \frac{\partial u}{\partial z} \right) &= \frac{3\eta_s}{S^2} \frac{\partial(S^2 u')}{\partial z} + \frac{1}{S^2} \frac{\partial[S^2(\tau_{zz} - \tau_{rr})]}{\partial z} \\ &\quad - \frac{\partial}{\partial z} \left\{ C \left[\sigma + \frac{\kappa_s - \mu_s}{S} \left(\frac{\partial(u S)}{\partial z} - \frac{C}{2} \frac{\partial(u S^2)}{\partial z} \right) \right] \right\} \\ &\quad + \frac{2}{S} \left\{ \frac{\partial \sigma}{\partial z} + \frac{\partial}{\partial z} \left[\frac{\kappa_s - \mu_s}{S} \left(\frac{\partial(u S)}{\partial z} - \frac{C}{2} \frac{\partial(u S^2)}{\partial z} \right) \right] \right\} \\ &\quad + \frac{5}{S^2} \frac{\partial}{\partial z} \left(\mu_s S \frac{\partial u}{\partial z} \right), \end{aligned} \tag{A43}$$

$$\tau_{zz} = \frac{\eta_p}{\lambda_c} \left(\frac{A_{zz}}{1 - \frac{tr(\mathbf{A})}{L^2}} - 1 \right), \tag{A44}$$

$$\tau_{rr} = \frac{\eta_p}{\lambda_c} \left(\frac{A_{rr}}{1 - \frac{tr(\mathbf{A})}{L^2}} - 1 \right), \tag{A45}$$

$$\frac{\partial A_{zz}}{\partial t} + u \frac{\partial A_{zz}}{\partial z} - 2 \frac{\partial u}{\partial z} A_{zz} = \frac{1}{\lambda_c} \left(1 - \frac{A_{zz}}{1 - \frac{tr(\mathbf{A})}{L^2}} \right), \tag{A46}$$

$$\frac{\partial A_{rr}}{\partial t} + u \frac{\partial A_{rr}}{\partial z} + \frac{\partial u}{\partial z} A_{rr} = \frac{1}{\lambda_c} \left(1 - \frac{A_{rr}}{1 - \frac{tr(\mathbf{A})}{L^2}} \right), \quad (\text{A47})$$

$$\frac{\partial \Gamma}{\partial t} + \frac{1}{S} \frac{\partial (Su\Gamma)}{\partial z} - \frac{C\Gamma}{2S} \frac{\partial (S^2u)}{\partial z} = D_s \frac{1}{S} \frac{\partial (S\Gamma')}{\partial z}, \quad (\text{A48})$$

where $tr(\mathbf{A}) = A_{zz} + 2A_{rr}$ and C , κ_s , μ_s and σ are given in (2.13) and (2.17a,b)–(2.18), respectively.

REFERENCES

- ALHUSHAYBARI, A. & UDDIN, J. 2020 Absolute instability of free-falling viscoelastic liquid jets with surfactants. *Phys. Fluids* **32**, 013102.
- ALSHARIF, A. 2019 Temporal and spatial instability of viscoelastic compound jets. *Eur. J. Mech. (B/Fluids)* **74**, 320–330.
- ALVAREZ, N.J., ANNA, S.L., SAIGAL, T., TILTON, R.D. & WALKER, L.M. 2012 Interfacial dynamics and rheology of polymer-grafted nanoparticles at air-water and xylene-water interfaces. *Langmuir* **28**, 8052–8063.
- ANNA, S.L. 2016 Droplets and bubbles in microfluidic devices. *Annu. Rev. Fluid Mech.* **48**, 285–309.
- ANSHUS, B.E. 1973 The effect of surfactants on the breakup of cylinders and jets. *J. Colloid Interface Sci.* **43**, 113–121.
- ARDEKANI, A.M., SHARMA, V. & MCKINLEY, G.H. 2010 Dynamics of bead formation, filament thinning and breakup in weakly viscoelastic jets. *J. Fluid Mech.* **665**, 46–56.
- BECK, V.A. & SHAQFEH, E.S.G. 2006 Ergodicity breaking and conformational hysteresis in the dynamics of a polymer tethered at a surface stagnation point. *J. Chem. Phys.* **124**, 094902.
- BHAT, P.P., APPATHURAI, S., HARRIS, M.T., PASQUALI, M., MCKINLEY, G.H. & BASARAN, O.A. 2010 Formation of beads-on-a-string structures during break-up of viscoelastic filaments. *Nat. Phys.* **6**, 625–631.
- BOUSSINESQ, J.V. 1913 Sur l'existence d'une viscosité superficielle, dans la mince couche de transition séparant un liquide d'un autre fluide contigu. *J. Ann. Chim. Phys.* **29**, 349–357.
- BRENN, G., LIU, Z. & DURST, F. 2000 Linear analysis of the temporal instability of axisymmetrical non-Newtonian liquid jets. *Intl J. Multiphase Flow* **26**, 1621–1644.
- CARROLL, C.P. & JOO, Y.L. 2006 Electrospinning of viscoelastic Boger fluids: modeling and experiments. *Phys. Fluids* **18**, 053102.
- CHANG, H.-C., DEMEKHIN, E.A. & KALADIN, E. 1999 Iterated stretching of viscoelastic jets. *Phys. Fluids* **11**, 1717–1737.
- CLASEN, C., EGGERS, J., FONTELOS, M.A., LI, J. & MCKINLEY, G.H. 2006a The beads-on-string structure of viscoelastic threads. *J. Fluid Mech.* **556**, 283–308.
- CLASEN, C., PLOG, J.P., KULICKE, W.-M., MACOSKO, M., SCRIVEN, L.E., VERANI, M. & MCKINLEY, G.H. 2006b How dilute are dilute solutions in extensional flows? *J. Rheol.* **50**, 849–881.
- CRASTER, R.V., MATAR, O.K. & PAPAGEORGIOU, D.T. 2002 Pinchoff and satellite formation in surfactant covered viscous threads. *Phys. Fluids* **14**, 1364–1376.
- CRASTER, R.V., MATAR, O.K. & PAPAGEORGIOU, D.T. 2003 Pinchoff and satellite formation in compound viscous threads. *Phys. Fluids* **15**, 3409–3428.
- CRASTER, R.V., MATAR, O.K. & PAPAGEORGIOU, D.T. 2009 Breakup of surfactant-laden jets above the critical micelle concentration. *J. Fluid Mech.* **629**, 195–219.
- DECHELETTE, A., CAMPANELLA, O., CORVALAN, C. & SOJKA, P.E. 2011 An experimental investigation on the breakup of surfactant-laden non-Newtonian jets. *Chem. Engng Sci.* **66**, 6367–6374.
- DINIC, J. & SHARMA, V. 2020 Power laws dominate shear and extensional rheology response and capillarity-driven pinching dynamics of entangled hydroxyethyl cellulose (HEC) solutions. *Macromolecules* **53**, 3424–3437.
- DRAVID, V., SONGSERMONG, S., XUE, Z., CORVALAN, C.M. & SOJKA, P.E. 2006 Two-dimensional modeling of the effects of insoluble surfactant on the breakup of a liquid filament. *Chem. Engng Sci.* **61**, 3577–3585.
- EGGERS, J. 1993 Universal pinching of 3D axisymmetric free-surface flow. *Phys. Rev. Lett.* **71**, 3458–3460.
- EGGERS, J. 1997 Nonlinear dynamics and breakup of free-surface flows. *Rev. Mod. Phys.* **69**, 865–929.
- EGGERS, J. & VILLERMAUX, E. 2008 Physics of liquid jets. *Rep. Prog. Phys.* **71**, 036601.

- ENTOV, V.M. & HINCH, E.J. 1997 Effect of a spectrum of relaxation times on the capillary thinning of a filament of elastic liquid. *J. Non-Newtonian Fluid Mech.* **72**, 31–53.
- FONTELOS, M.A. & LI, J. 2004 On the evolution and rupture of filaments in Giesekus and FENE models. *J. Non-Newtonian Fluid Mech.* **118**, 1–16.
- FULLER, G.G. & VERMANT, J. 2012 Complex fluid-fluid interfaces: rheology and structure. *Annu. Rev. Chem. Biomol. Engng* **3**, 519–543.
- GOLDIN, M., YERUSHALMI, J., PFEFFER, R. & SHINNAR, R. 1969 Breakup of a laminar capillary jet of a viscoelastic fluid. *J. Fluid Mech.* **38**, 689–711.
- GOREN, S.L. & GOTTLIEB, M. 1982 Surface-tension-driven breakup of viscoelastic liquid threads. *J. Fluid Mech.* **120**, 245–266.
- HAMEED, M. & MALDARELLI, C. 2016 Effect of surfactant on the break-up of a liquid thread: modeling, computations and experiments. *Intl J. Heat Mass Transfer* **92**, 303–311.
- HAMEED, M., SIEGAL, M., YOUNG, Y.-N., LI, J., BOOTY, M.R. & PAPAGEORGIOU, D.T. 2008 Influence of insoluble surfactant on the deformation and breakup of a bubble or thread in a viscous fluid. *J. Fluid Mech.* **594**, 307–340.
- HANSEN, S., PETERS, G.W.M. & MEIJER, H.E.H. 1999 The effect of surfactant on the stability of a fluid filament embedded in a viscous fluid. *J. Fluid Mech.* **382**, 331–349.
- HE, D. & WYLIE, J.J. 2021 Temporal instability of a viscoelastic liquid thread surrounded by another viscoelastic fluid in presence of insoluble surfactant and inertia. *J. Non-Newtonian Fluid Mech.* **288**, 104468.
- HERRADA, M.A., PONCE-TORRES, A., RUBIO, M., EGGERS, J. & MONTANERO, J.M. 2022 Stability and tip streaming of a surfactant-loaded drop in an extensional flow. Influence of surface viscosity. *J. Fluid Mech.* **934**, A26.
- HU, T., FU, Q. & YANG, L. 2020 Falling film with insoluble surfactants: effects of surface elasticity and surface viscosities. *J. Fluid Mech.* **889**, A16.
- JAMES, D.F. 2009 Boger fluids. *Annu. Rev. Fluid Mech.* **41**, 129–142.
- KAMAT, P.M., WAGONER, B.W., THETE, S.S. & BASARAN, O.A. 2018 Role of Marangoni stress during breakup of surfactant-covered liquid threads: reduced rates of thinning and microthread cascades. *Phys. Rev. Fluids* **3**, 043602.
- KUMAR, D., RICHTER, C.M. & SCHROEDER, C.M. 2020 Conformational dynamics and phase behavior of lipid vesicles in a precisely controlled extensional flow. *Soft Matt.* **16**, 337–347.
- LI, F. & HE, D. 2021 Dynamics of a viscoelastic thread surrounded by a Newtonian viscous fluid inside a cylindrical tube. *J. Fluid Mech.* **926**, A21.
- LI, F., YIN, X.-Y. & YIN, X.-Z. 2017 Oscillation of secondary droplets in an Oldroyd-B viscoelastic liquid jet. *Phys. Rev. Fluids* **2**, 013602.
- LIAO, Y.C., FRANCES, E.I. & BASARAN, O.A. 2006 Deformation and breakup of a stretching liquid bridge covered with an insoluble surfactant monolayer. *Phys. Fluids* **18**, 022101.
- LIU, Z. & LIU, Z. 2006 Linear analysis of three-dimensional instability of non-Newtonian liquid jets. *J. Fluid Mech.* **559**, 451–459.
- LUCASSEN, J. & VAN DEN TEMPEL, M. 1972 Longitudinal waves on visco-elastic surfaces. *J. Colloid Interface Sci.* **41**, 491–498.
- MANIKANTAN, H. & SQUIRES, T.M. 2017 Pressure-dependent surface viscosity and its surprising consequences in interfacial lubrication flows. *Phys. Rev. Fluids* **2**, 023301.
- MANIKANTAN, H. & SQUIRES, T.M. 2020 Surfactant dynamics: hidden variables controlling fluid flows. *J. Fluid Mech.* **892**, P1.
- MARTÍNEZ-CALVO, A., RIVERO-RODRÍGUEZ, J., SCHEID, B. & SEVILLA, A. 2020 Natural break-up and satellite formation regimes of surfactant-laden liquid threads. *J. Fluid Mech.* **883**, A35.
- MARTÍNEZ-CALVO, A. & SEVILLA, A. 2018 Temporal stability of free liquid threads with surface viscoelasticity. *J. Fluid Mech.* **846**, 877–901.
- MARTÍNEZ-CALVO, A. & SEVILLA, A. 2020 Universal thinning of liquid filaments under dominant surface forces. *Phys. Rev. Lett.* **125**, 114502.
- MARTÍNEZ NARVÁEZ, C.D.V., MAZUR, T. & SHARMA, V. 2021 Dynamics and extensional rheology of polymer-surfactant association complexes. *Soft Matt.* **17**, 6116–6126.
- MATHUES, W., FORMENTI, S., MCLLOY, C., HARLEN, O.G. & CLASEN, C. 2018 CaBER vs ROJER-different time scales for the thinning of a weakly elastic jet. *J. Rheol.* **62**, 1135–1153.
- MCGOUGH, R.T. & BASARAN, O.A. 2006 Repeated formation of fluid threads in breakup of a surfactant-covered jet. *Phys. Rev. Lett.* **96**, 054502.
- MONTANERO, J.M. & GAÑÁN-CALVO, A.M. 2020 Dripping, jetting and tip streaming. *Rep. Prog. Phys.* **83**, 097001.

- OZAN, S.C. & JAKOBSEN, H.A. 2019 On the role of the surface rheology in film drainage between fluid particles. *Intl J. Multiphase Flow* **120**, 103103.
- PONCE-TORRES, A., HERRADA, M.A., MONTANERO, J.M. & VEGA, J.M. 2016 Linear and nonlinear dynamics of an insoluble surfactant-laden liquid bridge. *Phys. Fluids* **28**, 112103.
- PONCE-TORRES, A., MONTANERO, J.M., HERRADA, M.A., VEGA, E.J. & VEGA, J.M. 2017 Influence of the surface viscosity on the breakup of a surfactant-laden drop. *Phys. Rev. Lett.* **118**, 024501.
- PONCE-TORRES, A., RUBIO, M., HERRADA, M.A., EGGERS, J. & MONTANERO, J.M. 2020 Influence of the surface viscous stress on the pinch-off of free surfaces loaded with nearly-inviscid surfactants. *Sci. Rep.* **10**, 16065.
- PRABHAKAR, R., PRAKASH, J.R. & SRIDHAR, T. 2006 Effect of configuration-dependent intramolecular hydrodynamic interaction on elastocapillary thinning and breakup of filaments of dilute polymer solutions. *J. Rheol.* **50**, 925–947.
- SCRIVEN, L.E. 1960 Dynamics of a fluid interface - equation of motion for Newtonian surface fluids. *Chem. Engng Sci.* **12**, 98–108.
- SINGH, N. & NARSIMHAN, V. 2021 Impact of surface viscosity on the stability of a droplet translating through a stagnant fluid. *J. Fluid Mech.* **927**, A44.
- SINGH, N. & NARSIMHAN, V. 2022 Numerical investigation of the effect of surface viscosity on droplet breakup and relaxation under axisymmetric extensional flow. *J. Fluid Mech.* **946**, A24.
- SUR, S. & ROTHSTEIN, J. 2018 Drop breakup dynamics of dilute polymer solutions: effect of molecular weight, concentration, and viscosity. *J. Rheol.* **62**, 1245–1259.
- TEMBELY, M., VADILLO, D., MACKLEY, M.R. & SOUCEMARIANADIN, A. 2012 The matching of a one-dimensional numerical simulation and experiment results for low viscosity Newtonian and non-Newtonian fluids during fast filament stretching and subsequent break-up. *J. Rheol.* **56**, 159–183.
- TIMMERMANS, M.-L.E. & LISTER, J.R. 2002 The effect of surfactant on the stability of a liquid thread. *J. Fluid Mech.* **459**, 289–306.
- TIRTAATMADJA, V., MCKINLEY, G.H. & COOPER-WHITE, J.J. 2006 Drop formation and breakup of low viscosity elastic fluids: effects of molecular weight and concentration. *Phys. Fluids* **18**, 043101.
- TURKOZ, E., LOPEZ-HERRERA, J.M., EGGERS, J., ARNOLD, C.B. & DEIKE, L. 2018 Axisymmetric simulation of viscoelastic filament thinning with the Oldroyd-B model. *J. Fluid Mech.* **851**, R2.
- VLAHOVSKA, P.M. 2019 Electrohydrodynamics of drops and vesicles. *Annu. Rev. Fluid Mech.* **51**, 305–330.
- WAGNER, C., AMAROUCHENE, Y., BONN, D. & EGGERS, J. 2005 Droplet detachment and satellite bead formation in viscoelastic fluids. *Phys. Rev. Lett.* **95**, 164504.
- WEE, H., WAGONER, B.W. & BASARAN, O.A. 2022 Absence of scaling transitions in breakup of liquid jets caused by surface viscosity. *Phys. Rev. Fluids* **7**, 074001.
- WEE, H., WAGONER, B.W., GARG, V., KAMAT, P.M. & BASARAN, O.A. 2021 Pinch-off of a surfactant-covered jet. *J. Fluid Mech.* **908**, A38.
- WEE, H., WAGONER, B.W., KAMAT, P.M. & BASARAN, O.A. 2020 Effects of surface viscosity on breakup of viscous threads. *Phys. Rev. Lett.* **124**, 204501.
- WODLEI, F., SEBILLEAU, J., MAGNAUDET, J. & PIMENTA, V. 2018 Marangoni-driven flower-like patterning of an evaporating drop spreading on a liquid substrate. *Nat. Commun.* **9**, 820.
- YAO, M., YANG, L. & FU, Q. 2021 Temporal instability of surfactant-laden compound jets with surface viscoelasticity. *Eur. J. Mech. (B/Fluids)* **89**, 191–202.
- YE, H., YANG, L. & FU, Q. 2016 Instability of viscoelastic compound jets. *Phys. Fluids* **28**, 043101.
- YOUNG, Y.-N., BOOTY, M.R., SIEGEL, M. & LI, J. 2009 Influence of surfactant solubility on the deformation and breakup of a bubble or capillary jet in a viscous fluid. *Phys. Fluids* **21**, 072105.
- ZELL, Z.A., NOWBAHAR, A., MANSARD, V., LEAL, L.G., DESHMUKH, S.S., MECCA, J.M., TUCKER, C.J. & SQUIRES, T.M. 2014 Surface shear inviscidity of soluble surfactants. *Proc. Natl Acad. Sci.* **111**, 3677–3682.